NONLINEAR OPTICAL EFFECTS ON RETINAL DAMAGE THRESHOLDS

IN THE 1200-1400 nm WAVELENGTH RANGE

A Dissertation

by

FRANCESCO JOZAC ECHEVERRIA

Submitted to the Office of Graduate and Professional Studies
Texas A&M University
in partial fulfillment of the requirements for the degree of

DOCTOR OF PHILOSOPHY

Chair of Committee,	Alexei Sokolov
Committee Members,	Edward Fry
	George Kattawar
	Benjamin Wherley
Head of Department,	George Welch

May 2015

Major Subject: Applied Physics

ABSTRACT

Recent changes in the maximum permissible exposure (MPE) limits for near-infrared (NIR) laser exposures are analyzed in light of nonlinear optical phenomena. We have evaluated the thresholds for supercontinuum (SC) generation for ultra-short (femtosecond) laser exposures in the NIR region and compared these values with the MPEs listed in the *American National Standard for Safe Use of Lasers* 2014 Edition (ANSI Z136.1-2014). Due to the strong increase in ocular absorption in the 1.2 to 1.4 micrometer (i.e. 1200-1400 nm) range, evaluation of the SC generation phenomenon is necessary because any shift in laser energy within the eye to shorter wavelengths (i.e. greater frequency) could lead to unforeseen increases in hazards to the retina. The findings of this research do in fact indicate a shift in laser energy to shorter wavelengths for femtosecond pulsed lasers. In addition, an analysis involving spectral measurements through a water cuvette leads to estimations involving the eye configuration that show radiant exposures exceeding the ANSI thresholds for visible wavelengths. The implications of these findings are such that enough NIR energy is converted to visible energy near the retina when dealing with femtosecond pulsed lasers, warranting further studies in examining what the effects caused by nonlinear optical phenomena due to ultrashort pulsed lasers have on MPE thresholds established for eye safety.

DEDICATION

To my parents, brothers, and sister, who built me up with the courage and confidence to

take on such a task as a PhD in Applied Physics. To my wife and three children, for you

I always want to be a better man. To my Heavenly Father, for Your glory and grace is

how I have managed to continue through this life to serve Your purpose.

ACKNOWLEDGEMENTS

TABLE OF CONTENTS

LIST OF FIGURES

LIST OF TABLES

CHAPTER I

INTRODUCTION

1.1   MOTIVATION AND OBJECTIVE

In March of 2014, the ANSI Z136.1 laser safety standard was reissued with

mostly evolutionary changes included [1]. Some of the revolutionary changes were

changes to the maximum permissible exposure (MPE) levels, specifically in the 1.2-1.4

µm (i.e. 1200-1400 nm) wavelength range. In this range, some MPEs increased by

factors of several thousand, the most significant changes to exposure levels in modern

history [2]. As an example, the MPEs for one nanosecond exposures are compared for

the 2007 and 2014 standards in Figure 1.1.

The significant change in exposure levels is warranted based on minimum visible

lesion (MVL) data collected over the past decade [2-11] in the nanosecond to seconds of

exposure range. The MPEs in the 1200-1400 nm range changed for exposure durations

from 100 femtosecond (fs) to 30,000 sec. The topic of this study is the evaluation of the

MPEs for 30 to 40 fs exposure durations in the 1200-1400 nm wavelength range.

For femtosecond exposures, nonlinear optical processes are possible and can

dominate the resulting damage mechanisms [12]. The nonlinear optical phenomena

implicated in threshold retinal damage are self-focusing and laser-induced breakdown.

These nonlinear optical phenomena [13] are more significant as pulse duration is

decreased below 100 ps. Other nonlinear optical phenomena were evaluated as non-

contributing effects to threshold laser damage in the visible spectrum [14].
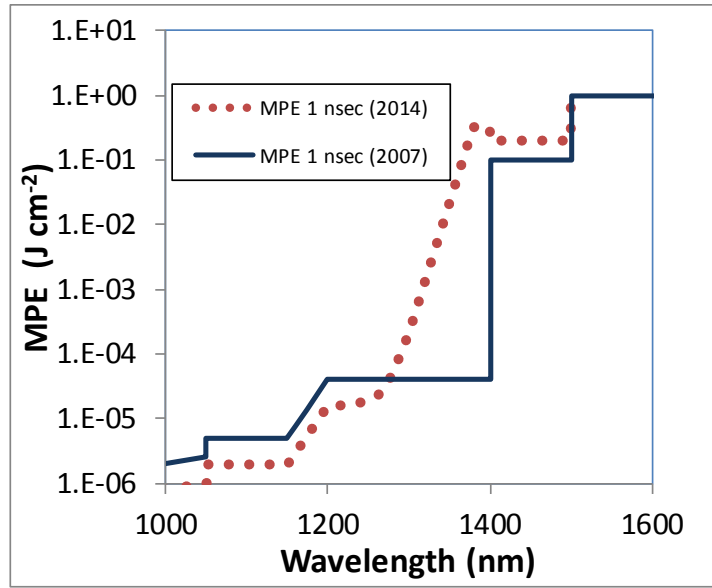
FIGURE 1.1 Maximum permissible exposure limits for the near-infrared wavelength region for the 2007 and 2014 ANSI Z136.1 laser safety standards.

For 100 fs exposures, the MPE is given for point sources as $C_C \times 10^{-7}$ J·cm^{-2}, where C_C is defined as the wavelength dependent correction factor [15]. This appears to be a very small MPE based on the sub-microjoule per centimeter-squared factor. Upon inspection of C_C, one can see that this correction factor increases to one million ($C_C = 10^{0.018(\lambda-1150)}$ for 1150 nm $< \lambda <$ 1200 nm and $C_C = 8 + 10^{0.04(\lambda-1250)}$ for 1200 nm $< \lambda <$ 1400 nm), and hence dramatically increases the radiant exposure for 100 fs exposures in the NIR region [15]. Therefore in this NIR region, there can be exposure in the range of 1 mJ cm^{-2} for the 1.2-1.4 μm wavelength range.

The purpose of this research is to determine if there are nonlinear effects that occur in the 30-40 fs pulse duration range that may cause re-examination of previously established eye-safe laser standards in the 100 fs duration range. The results of this

2

research will directly impact the analysis of the current ANSI standards, specifically, the maximum permissible exposure (MPE) thresholds established for the near infrared region (NIR) ranging from 1200-1400 nm. In order to conduct this research, it was necessary to create a device that generated the tunable laser light from 1150-1600 nm. This was done by the use of a non-collinear optical parametric amplifier (NOPA). The NOPA generated light amplification at 1300 nm, which was tunable to 1150 and 1600 nm. At this point we were able to send the desired wavelength through a cuvette filled with distilled water. The purpose of the water filled cuvette was to demonstrate that a laser-induced nonlinear phenomenon known as supercontinuum (SC) generation occurred via the use of femtosecond pulses in the NIR region at a measured energy per pulse and repetition rate. After SC generation was observed in the water filled cuvette set up, an analysis was conducted to estimate the radiant exposure values using established approximate dimensions of the eye. A comparison was made to establish whether the current ANSI laser safety standards are in need of consideration of nonlinear optical phenomena such as SC generation via self-phase modulation (SPM).

This study presents measurements and analysis to relate the retinal damage threshold to the increased MPEs. The objective of this study is to show that the current American National Standard (ANSI) maximum permissible exposure thresholds for laser eye safety could be significantly lower in the 1200-1400 nm wavelength range for laser pulses in the femtosecond duration range. Laser safety in the laboratory environment must be reassessed to determine the appropriate measures such as laser eye protection to prevent retinal damage.

1.2 OUTLINE

This dissertation provides a logical argument for reassessing the current ANSI standard for laser eye safety in the 1200-1400 nm wavelength range. Introductory material is intended to provide a relevant perspective of the studied range of wavelengths within the electromagnetic spectrum. In addition, a brief discussion on why the NIR region is preferred in laser applications is made to illustrate the significance of this research. Theoretical equations will be presented where necessary, in particular when the discussion turns to the nonlinear effects responsible for considering the changes in MPEs for specific wavelengths in the NIR region. The data acquired in the laboratory analyzes the interaction of femtosecond pulses in water, which is then used to extrapolate assumptions and approximations with femtosecond pulses interacting with the human eye. No biological samples or animals were used in conducting this experiment.

CHAPTER II

ELECTROMAGNETIC WAVES, VISIBLE LIGHT, EMISSION SPECTRUM, AND

CHOOSING NIR LASER APPLICATIONS

2.1   ELECTROMAGNETIC WAVES AND VISIBLE LIGHT

The electromagnetic (EM) spectrum covers a wide range of frequencies and

wavelengths that are typically not associated with visible light outside the scientific

community. In reality, visible light is made of the same fluctuating electric and

magnetic fields that make up the entire spectrum ranging from gamma rays, which have

frequencies on the order of 10^{20} Hz (that is one hundred million trillion), to radio

frequencies (RF) having frequencies on the order of 10^6 Hz. The relation that links

frequency and wavelength is given by the following:

$$c = \lambda\nu \qquad\qquad (2.1)$$

where λ is the wavelength, ν is the frequency, and c is the speed of light in a vacuum.

From this equation, it is easy to see that wavelength and frequency are inversely

proportional given that the speed of light is constant. In addition, EM radiation travels

through space as bundles of energy known as photons. The energy that photons carry is

directly proportional to the frequency, inversely proportional to the wavelength, of the

EM radiation propagating, which is given by the following relationship in terms of

frequency:

$$E = h\nu \qquad\qquad (2.2)$$

where h is known as Planck's constant and E is the energy that the radiated photon carries. While the term photon is typically not used for frequencies and wavelengths beyond the infrared (IR) region, the term photon is certainly not restricted to the EM spectrum ranging from gamma rays to the IR region. In this study, we will commonly use wavelength in describing the various types of propagated laser light used in our experiment. A couple of things to keep in mind is the relationship that the wavelength of the propagated light has with its frequency and energy of the photon in which it propagates. It is important to realize that a photon of shorter wavelength has a greater frequency and consequently greater energy than a photon of longer wavelength. This will be particularly important when we discuss the nonlinear effects of a femtosecond pulse of NIR light through water. The specific wavelength range that the average human sees, what is referred to as the visible region of the EM spectrum, ranges from 400 nm to 700 nm. The wavelength that is the primary focus of the data acquired via experimentation ranges from 1200 nm to 1400 nm. Figure 2.1 illustrates the position of the 1200 to 1400 nm range. Note the location of the narrow wavelength range of 1200 to 1400 nm, which is slightly greater than 1 μm (1000 nm), or 10^{-6} meters.
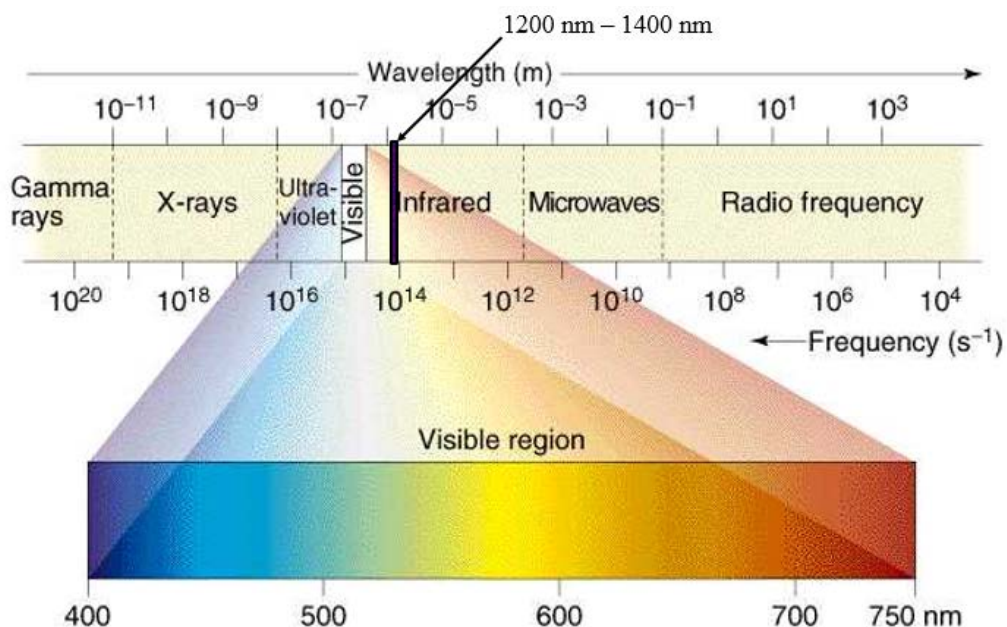
FIGURE 2.1 The electromagnetic spectrum. Figure taken from CHEMISTRY: The Central Science 7/e by Brown/LeMay/Bursten, Copyright 1997 by Prentice-Hall, Inc. Simon & Schuster/ A Viacom Company, Upper Saddle River, NJ 07458.

2.2   EMISSION SPECTRUM

When people outside the scientific community think of light of a specific color such as blue, yellow, green, or red, they often think of that specific wavelength. In reality, when an object emits or reflects a certain color or wavelength, the object is actually emitting or reflecting many wavelengths, known as an emission spectrum. When an object emits a primary wavelength with a few side bands either less than or greater than the primary wavelength, the band width is said to be narrow, or the source has a narrow emission spectrum. Lasers that are coherent and monochromatic are said to have narrow emission spectrums. When an object emits radiation with a wide range of wavelengths (or frequencies), the object is said to have a broad band width, or have a

7

wide emission spectrum. Figure 2.2 illustrates the emission spectrum of the sun outside
the earth atmosphere and at sea level. The spectrum of the sun encompasses a wide
range of radiated EM wavelengths, with the greatest flux emitted in the visible and the
NIR. Also evident in the figure are the transmission windows for specific wavelengths
within the atmosphere.
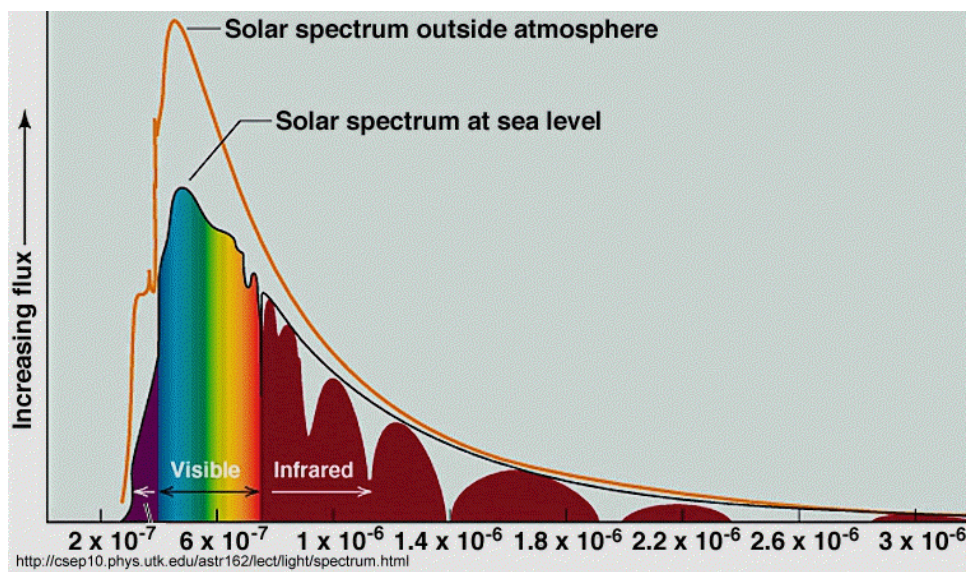
FIGURE 2.2 The solar spectrum [41].

In addition, however, there is still a substantial amount of NIR radiation emitted
from the sun. While the solar emission spectrum drops off quickly and smoothly in the
far infrared (FIR) region outside the atmosphere, the solar spectrum does not drop off
smoothly when measured at sea level. Comparing the solar spectrum outside the earth
atmosphere with the measured emission spectrum at sea level shows the EM
transmission windows within the earth atmosphere. While the visible spectrum is still

8

dominant at sea level, the visible spectrum shows the biggest drop in flux as the solar radiation propagates through the atmosphere. This is especially true for the shorter (blue) visible wavelengths. This is a result of a type of scattering known as Rayleigh scattering.

In 1871, Lord Rayleigh analyzed scattered sunlight via the oscillations of molecules and concluded, through dimensional analysis, that scattered light involving particles smaller than approximately $1/15^{th}$ the wavelength, λ, was scattered proportional to λ^{-4}, which meant that the intensity of the scattered light increased with ν^4, which has since then been referred to as Rayleigh scattering. Rayleigh scattering very much, in part, explains why the sky appears blue. Consider a narrow beam of sunlight which has in it a broad range of frequencies propagating through the atmosphere. As the beam moves through the atmosphere, it collides with molecules in the air (e.g. nitrogen, oxygen, etc.). As the beam collides with the molecules in the atmosphere, which primarily consists of nitrogen and oxygen with diameters of a few tenths of a nanometer, the shorter wavelength blue light gets scattered more appreciably (especially for longer path lengths) than the longer wavelength orange and red light, which explains the fiery sunsets on the surface of the Earth [18], and the significant drop in the visible emission spectrum from outside the atmosphere to sea level in Figure 2.2. One important thing to note about Rayleigh scattering is that the scattering is done by elastic collisions of the photons with the atoms and molecules, which means that scattered photons have the same energy (frequency and wavelength) as the incident photons [19].

9

Figure 2.2 also illustrates that certain wavelengths propagate through the atmosphere without much attenuation (i.e. absorption or scattering). Solar radiation with wavelength approximately equal to 1.65 µm, for example, measured at sea level is approximately equal to the flux of that wavelength outside the atmosphere, indicating a high percentage of transmission (low attenuation) of EM radiation for that wavelength. Conversely, solar radiation with wavelength 1.4 µm is almost completely attenuated by the atmosphere, as shown in Figure 2.2.

2.3   WHY NIR LASER APPLICATIONS?

Since the invention of lasers in the 1960s [24], the military and private industry have sought ways to use the propagation of EM waves in a variety of ways, particularly in communication and non-lethal applications. From section 2.2, we begin to understand that choosing the wavelengths of interest cannot be random. One must consider how the particular propagated wavelength will interact as it travels through the atmosphere, especially when considering long distances. In Figure 2.3, we can see that the atmosphere is very opaque to certain parts of the EM spectrum such as gamma rays, X-rays, ultraviolet (UV) rays, some NIR, most FIR, and long-wavelength radio waves. From section 2.2 and Figure 2.3, we see that the visible, some NIR, and radio waves are very transparent in the earth atmosphere. The atmosphere is an open window to radio waves, which are primarily used in communications. Due to Rayleigh scattering experienced by the visible EM spectrum and the inherently low "photon" energy of radio

waves, the few NIR wavelengths that are relatively transparent are generally preferred,

especially when considering long distance propagation.
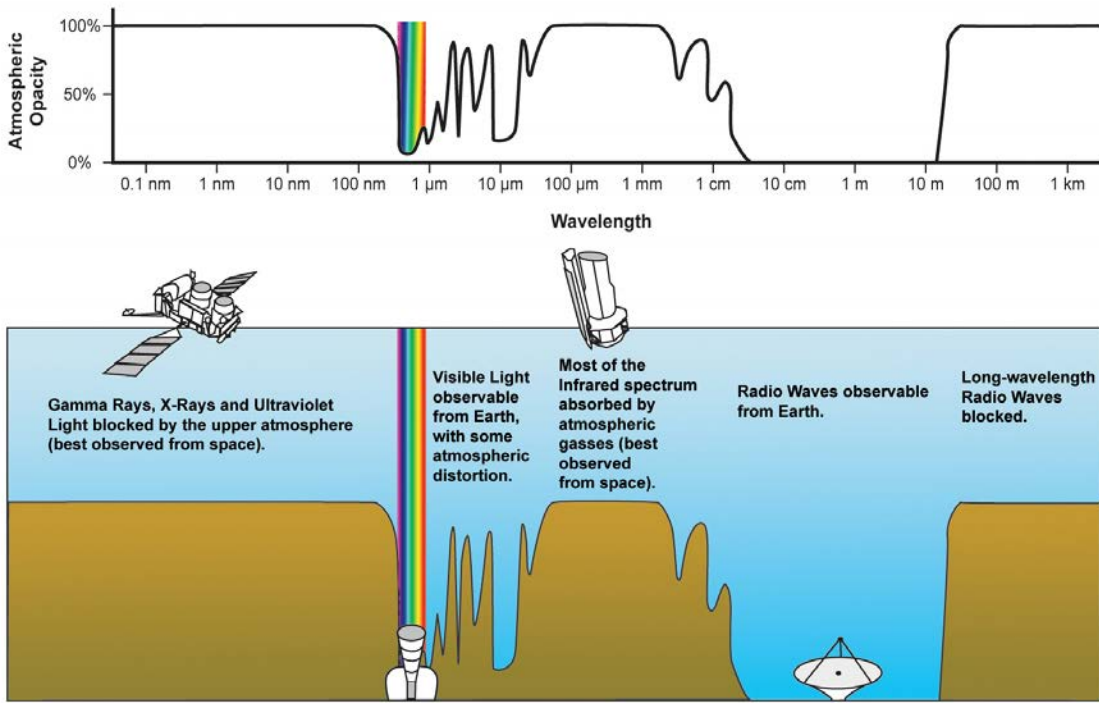
FIGURE 2.3 Atmospheric opacity [42].

CHAPTER III

NONLINEAR OPTICAL PHENONMENA, SUPERCONTINUUM (SC)

GENERATION, SPECTRAL BROADENING, AND SELF PHASE MODULATION

(SPM)

3.1   NONLINEAR OPTICAL PHENOMENA

In the same way that a classical spring, which typically demonstrates a linear

relationship between force and displacement, can be overdriven into a nonlinear

response (inelastic distortion of the spring material) by applying a strong enough force,

the propagation of light, which typically assumes a linear relationship (through

superposition, reflection, and refraction) between the oscillating EM field and the atoms

in the interacting medium, can be overdriven by extremely intense beams (such as high

energy lasers) to generate significant nonlinear effects [25]. Stimulated Brillouin

Scattering, for example, is caused when the variations in the electric field of an intense

beam traveling in a medium produces acoustic vibrations within the medium, resulting in

scattered photons of the same wavelength (and frequency) in the opposite direction of

the incoming beam [26]. Self-focusing, another nonlinear effect, also occurs when a

medium is exposed to an intense amount of EM radiation. The intense radiation causes

the refractive index of the medium to increase, resulting in the medium acting as a

focusing lens. The peak intensity, primarily located in the self-focusing region,

continues to increase as the beam travels through the medium until the process is

interrupted by damage to the medium caused by the super focused, even more highly

intense beam [27]. Harmonic generation, which is also typically caused by intense focused laser radiation, is a nonlinear phenomenon that converts radiation from one frequency (or wavelength) to a higher harmonic of the original frequency [28]. As Figure 3.1 illustrates, harmonic generation results in a conversion of incoming radiation interacting with a medium to radiation with shorter wavelength multiples of the original wavelength. Figure 3.1 is a specific type of harmonic generation known as second harmonic generation (SHG). In this illustration, incoming photons with wavelength 1064 nm (NIR) interact with a medium. Exiting the medium are photons with wavelength 532 nm (visible green), half the wavelength of the incoming 1064 nm or twice the frequency of the incoming photon.

SHG is called as such because it converts two incoming photons with identical photon energy to one outgoing photon with the same photon energy as the incoming two photon combination. For SHG, photons with wavelength 1064 nm (for example) interact with a medium and result in photons with wavelength 532 nm exiting the medium. The exiting photons with half the wavelength (532 nm) of the incoming photons (1064 nm) will have exactly twice the frequency, from Equation 2.1, and twice the photon energy, from Equation 2.2, as the individual incoming photons. As mentioned earlier, SHG is one specific kind of harmonic generation. It is also possible to have third harmonic generation (THG) and higher (i.e. fourth, fifth. etc.), where in THG three incoming photons are converted to one outgoing photon with three times the frequency and photon energy (one-third the wavelength) as one of the incoming photons.
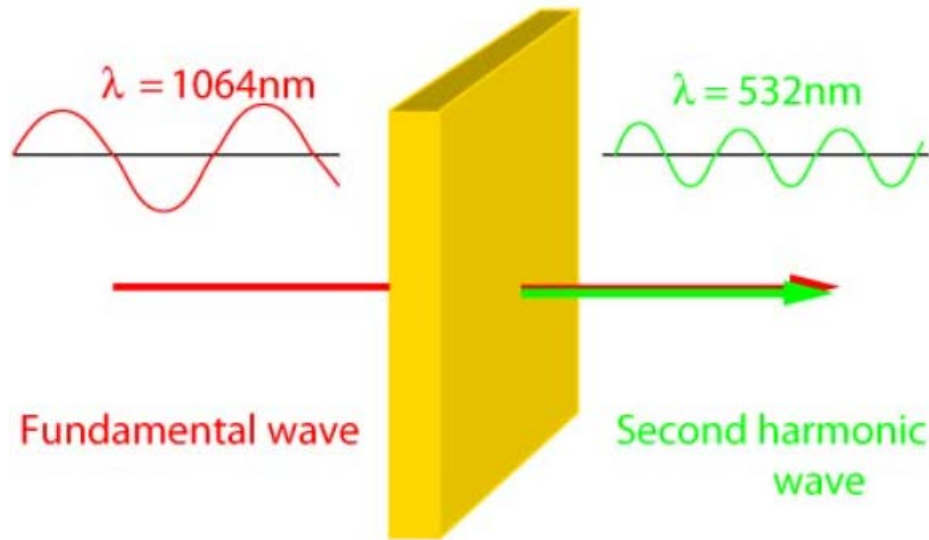
FIGURE 3.1 Second harmonic generation (SHG).

3.2   SUPERCONTINUUM (SC) GENERATION AND SPECTRAL BROADENING

Another nonlinear phenomenon driven by intense radiation is called

supercontinuum (SC) generation. SC generation is the process for which laser radiation

interacts with a medium and is converted to EM radiation with a very broad spectral

bandwidth within the medium, having many frequencies and wavelengths upon exiting

the medium. For example, Figure 3.2 shows a laser pulse with wavelength centered at

800 nm, temporal pulse width of approximately 50 fs, and peak power of 10 kW. As the

pulse interacts with the medium, the temporal pulse width of approximately 50 fs

remains virtually unchanged. The spectrum, however, has been broadened with

components having wavelengths ranging from the visible spectrum to the NIR, from

approximately 450 nm – 1400 nm, indicating a large amount of spectral broadening.

Temporal Pulseshape of Input

Temporal Pulseshape of Output

Spectrum of Input

Spectrum of Output

Input pulse: 50 fs,   800 nm,   10 kW peak power
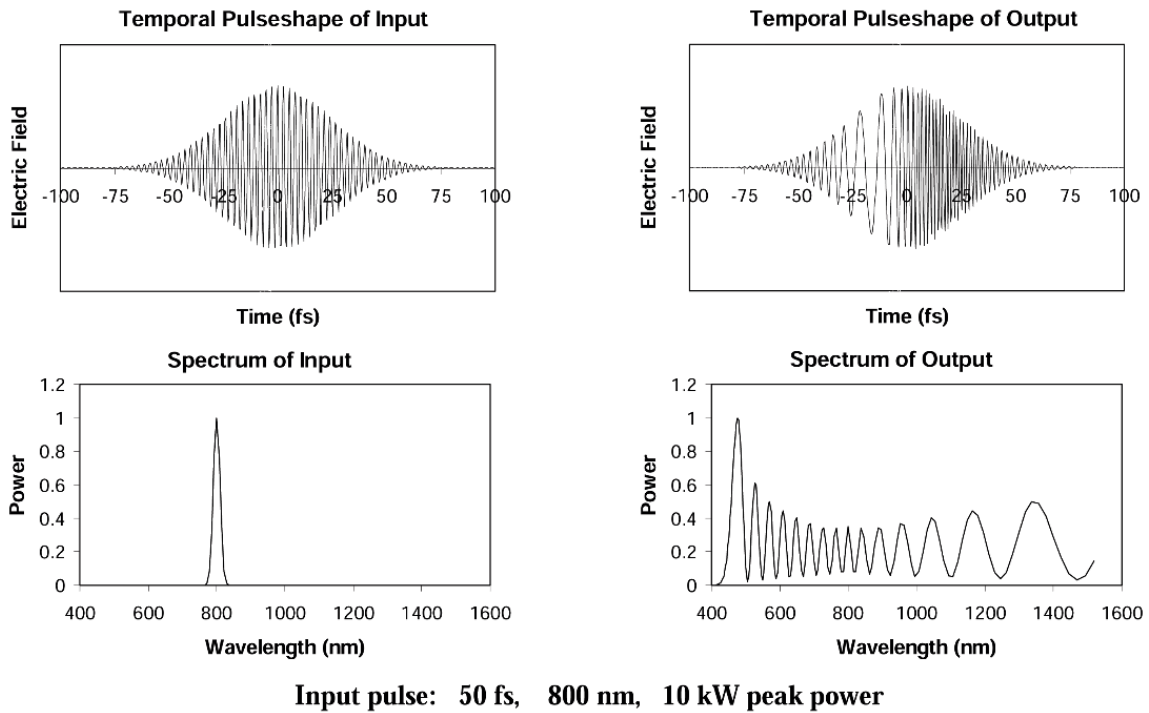
FIGURE 3.2 SC Generation and spectral broadening.

The spectral broadening, which occurs within the medium itself, generates higher energy photons in the visible spectrum, especially around 450 nm. In addition, the output spectrum does not just include wavelengths that are less than the incoming pulse wavelength of 800 nm, which is in the very NIR. The spectrum can also include wavelengths deep into the NIR region (and perhaps into the FIR), as shown in Figure 3.2. Lastly, observing the temporal pulse shape at the output, we can see that the wavelength of the fluctuating electric field within the 50 fs pulse is not constant, as the pulse was prior to interacting with the medium at a wavelength approximately 800 nm. Observe that the leading portion of the temporal pulse is down shifted in frequency (red-shifted), while the trailing portion of the pulse is up shifted (blue-shifted). The red

15

shifting can be thought of as a stretching of the fluctuating electric field while the blue

shifting can be thought of as a compressing of the fluctuating electric field within the

temporal pulse width, which remains unchanged at 50 fs at the output for the example

shown in Figure 3.2. When femtosecond pulses are used, spectral broadening is

typically dominated by a process known as self-phase modulation (SPM) [29].

3.3   SELF-PHASE MODULATION (SPM)

          Self-phase modulation (SPM) is the process that often dominates the spectral

broadening that occurs when a femtosecond pulse interacts with a nonlinear material.

Figure 3.3 shows an example of an un-chirped pulse (i.e. a pulse where the electric field

fluctuations are constant within the pulse) interacting with a positive medium (i.e.

positive index of refraction) and resulting in a chirped, spectrally broadened, pulse.
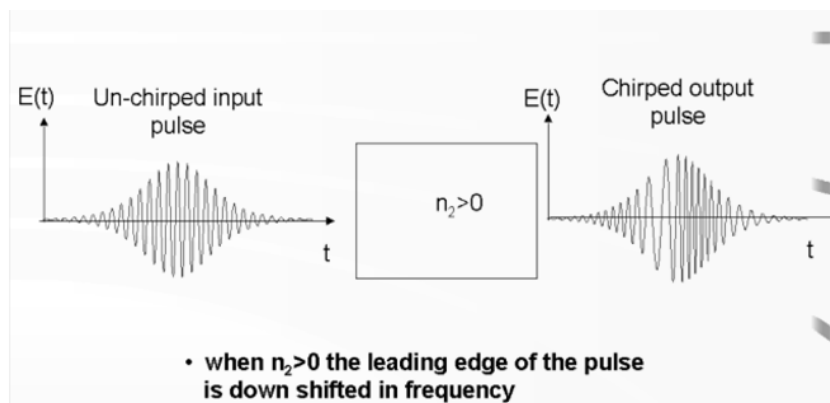
FIGURE 3.3 Self-Phase Modulation (SPM).

We can see that the result of the un-chirped pulse, presumably several femtoseconds in

duration, interacting with a medium and undergoing SPM, is a chirped pulse where the

leading portion of the pulse is positively chirped and the trailing portion is negatively

chirped. The result is the spectral broadening, where the measured spectrum indicates

the various wavelengths caused by the chirping of the SPM process. The mathematical

process describing SPM is best explained by first considering a pulse with an assumed

Gaussian shaped intensity profile, such as the one shown in Figure 3.4. Notice how the

leading edge of the pulse corresponds to lower (negative) frequency shift values and the

trailing edge of the pulse corresponds to higher (positive) frequency shifts. The peak

intensity does not cause a shift in the initial frequency ω_0.
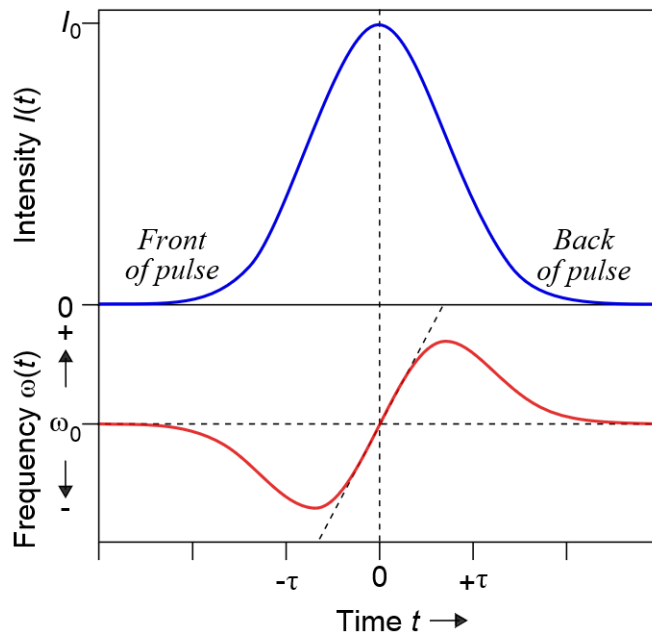
FIGURE 3.4 General example of a pulse with a Gaussian shaped intensity profile and
instantaneous frequency shift $\omega(t)$ plotted below.

The equation for the intensity with a Gaussian shaped profile is as follows:

$$I(t) = I_0 e^{-t^2/\tau^2} \qquad (3.1)$$

where I_0 is the peak intensity, t gives the intensity at any given time and τ is half the pulse duration. When the pulse interacts with a medium, the optical Kerr effect produces a change in the refractive index as a function of the intensity $I(t)$ given by the following:

$$n(t) = n_0 + n_2 I(t) \qquad (3.2)$$

where n_0 and n_2 are the linear and nonlinear (second order) indices of refraction of the medium, respectively. The optical Kerr effect, or AC Kerr effect, is caused by an intense beam of light interacting with a medium, which itself causes the modulation of the fluctuating electric field [30]. The result of which is Equation 3.2, where the index of refraction now varies proportionally to the time varying intensity of the beam as it propagates through the medium. As the pulse in Figure 3.4 propagates through the medium in time, the intensity at any given cross section within the beam will rise and fall as the beam propagates. This will cause very quick time variances of the index of refraction in the medium. The time varying index of refraction is expressed by the following derivative:

$$\frac{dn(t)}{dt} = n_2 \frac{dI(t)}{dt} \qquad (3.3)$$

Applying Equation 3.3 to Equation 3.2, we get the following:

$$\frac{dn(t)}{dt} = n_2 \left(\frac{-2I_0 t}{\tau^2} \right) e^{-t^2/\tau^2} \qquad (3.4)$$

which represents the equation for the time-varying refractive index. This variation of refractive index (Equation 3.4) will produce a shift in the instantaneous phase of the pulse given by:

18

$$\varphi(t) = \omega_0 t - kx = \omega_0 t - \frac{2\pi}{\lambda_0} n(t) L \tag{3.5}$$

where ω_0 and λ_0 are the frequency and wavelength of the pulse prior to interacting with the medium (i.e. in air or in a vacuum), and L is the distance that the pulse has propagated in the medium. Any instantaneous phase shift will result in an instantaneous frequency shift given by the following:

$$\omega(t) = \frac{d\varphi(t)}{dt} \tag{3.6}$$

Applying Equation 3.6 to Equation 3.5 therefore results in:

$$\omega(t) = \omega_0 - \frac{2\pi L}{\lambda_0} \frac{dn(t)}{dt} \tag{3.7}$$

By substituting Equation 3.4 into Equation 3.7, we arrive at the following equation for the instantaneous frequency shift:

$$\omega(t) = \omega_0 - \frac{2\pi L n_2}{\lambda_0} \left(\frac{-2I_0 t}{\tau^2} \right) e^{-t^2/\tau^2} = \omega_0 + \frac{4\pi L n_2 I_0 t}{\lambda_0 \tau^2} e^{-t^2/\tau^2} \tag{3.8}$$

which is shown plotted below the Gaussian intensity curve in Figure 3.4. Notice that the frequency shift curve is negative for the front portion of the pulse, indicating a shift to lower frequencies or longer wavelengths, while the back portion of the pulse corresponds to positive frequencies, indicating a shift to higher frequencies or shorter wavelengths. At the center of the pulse, where the intensity is maximum (i.e. I_0), the frequency is not shifted at all. Also note that at the center portion of the beam, when $t \approx {}^+_- \tau/2$, the frequency shift is approximately linear from lower to higher frequencies (longer to shorter wavelengths) as the pulse moves through any point in the medium [31]. We must note that the maximum and minimum values for $\omega(t)$, which can be calculated by taking the derivative of Equation 3.8 with respect to time t and evaluating

19

when the derivative is equal to zero, indicate the maximum and minimum frequencies

attained in the spectral broadening of the initial frequency ω_0. These frequencies can

certainly be converted to maximum and minimum wavelengths observed in the spectral

broadening by using Equation 2.1.

CHAPTER IV

THE EYE, WATER ABSORPTION, AND OCULAR TRANSMISSION

4.1   THE EYE

The human eye is a very complex organ that has different critical components

especially susceptible to biological damage by EM radiation. The critical components of

the eye responsible for focusing an image of an object to the retina are the cornea,

aqueous humor, lens, and the vitreous humor. Of these components, the cornea, lens,

and retina are the most susceptible to laser damage. When EM radiation enters the eye,

the radiation interacts (chronologically) with the cornea, aqueous humor, lens, vitreous

humor, and then the retina. Not all EM radiation reaches the retina, however, due to the

optical absorption in the outer components of the eye. The different optical components

of the eye absorb and transmit different amounts of EM radiation depending on the

wavelength of the EM radiation entering the eye. The cornea, for example, absorbs most

far ultraviolet (FUV) radiation with wavelengths ranging from 100 nm to 315 nm and

FIR radiation with wavelengths ranging from 1400 nm to 1 mm. Any damage

experienced by the cornea due to FUV radiation typically results in a condition called

keratocojunctivitis, commonly referred to as snow blindness or welder's flash, and can

occur if significantly high doses of FUV radiation are absorbed. Overexposure to FIR

radiation most often results in corneal burns. Near ultraviolet (NUV) radiation with

wavelengths ranging from 315 nm to 400 nm is mostly absorbed in the lens of the eye,

which exists just past the cornea and aqueous humor shown in Figure 4.1. EM radiation

entering the eye interacts with the cornea, aqueous humor, lens, and vitreous humor

before reaching the retina. The EM radiation reaching the retina depends on the

wavelength of the EM radiation entering the eye. Damage caused by NUV radiation

usually goes undetected and does not occur for several years, usually resulting in

cataracts forming on the lens. The cornea and lens, however, are mostly transparent to

visible and NIR radiation with wavelengths ranging from 400 nm to 1400 nm. This

specifically means that any visible and NIR radiation entering the eye will propagate

through the cornea, aqueous humor, lens, and vitreous humor, where the radiation will

then be focused to the retina by the cornea and the lens, which acts like a positive

convex lens. Any amount of overexposure to the retina can lead to flash blindness or

retinal burns and lesions, resulting in severe long term vision problems [32].
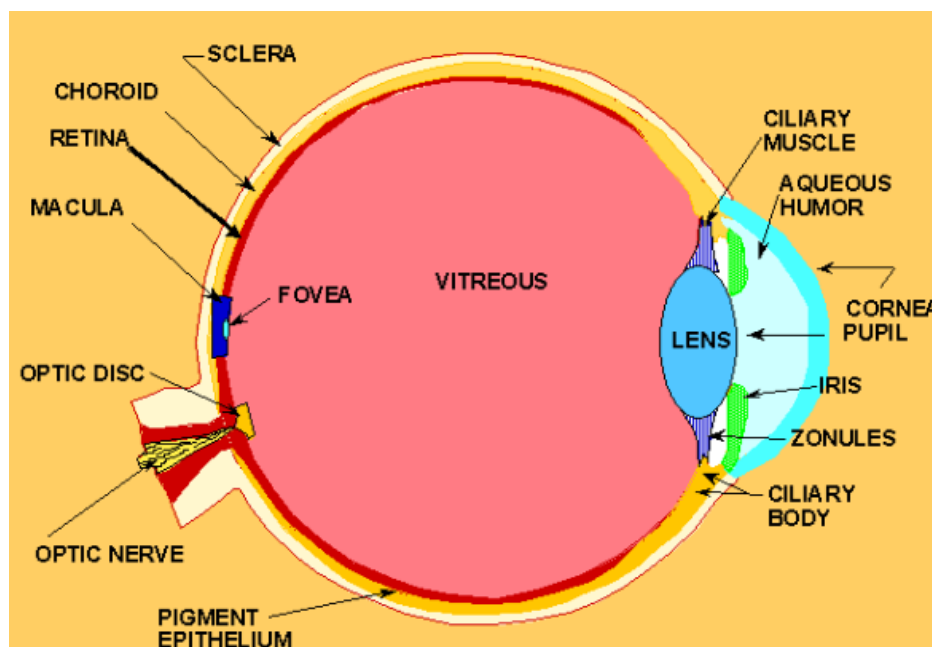
FIGURE 4.1 Schematic diagram of the human eye [43].

Figure 4.2 illustrates the EM spectrum of interest with regard to laser safety. Only the visible and NIR wavelengths ranging from 400 – 1400 nm pass through the eye structure and are focused on the retina. UV and FIR radiation with wavelengths ranging from 100 – 400 nm and 1400 – 1 mm, respectively, are highly absorbed by the cornea and lens.

Microwaves and Gamma Rays   **Near Ultraviolet**

Far Ultraviolet and Far Infrared   **Visible and Near Infrared**
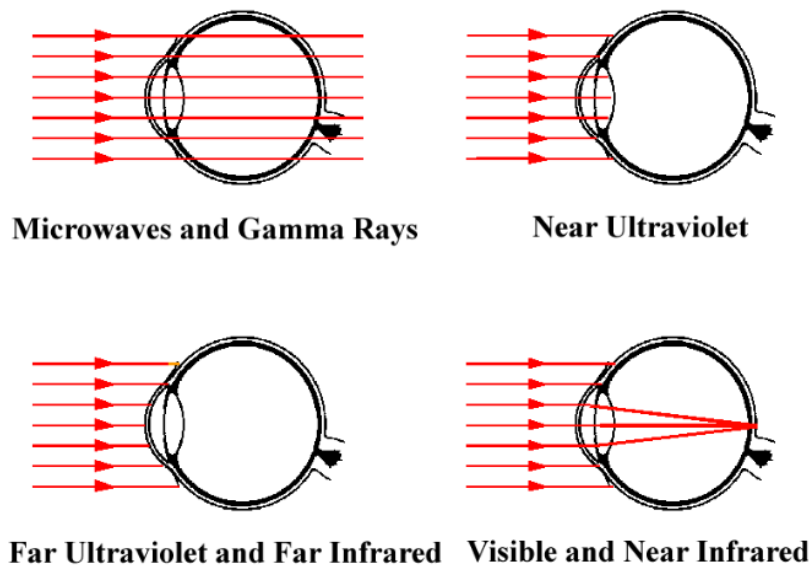
FIGURE 4.2 EM spectrum of interest with regard to laser safety [43].

4.2   WATER ABSORPTION AND OCULAR TRANSMISSION

Different materials absorb EM radiation at different rates depending on the wavelength. Water, for example, is very transparent to visible light, but highly absorbing of FIR radiation. Figure 4.3 shows the absorption coefficient for water over a large portion of the EM spectrum with wavelengths ranging from 10 nm to 10 mm. The absorption coefficient is minimum for EM radiation with a wavelength of approximately 525 nm, where the coefficient is approximately equal to 1.21×10^{-3} cm^{-1}.
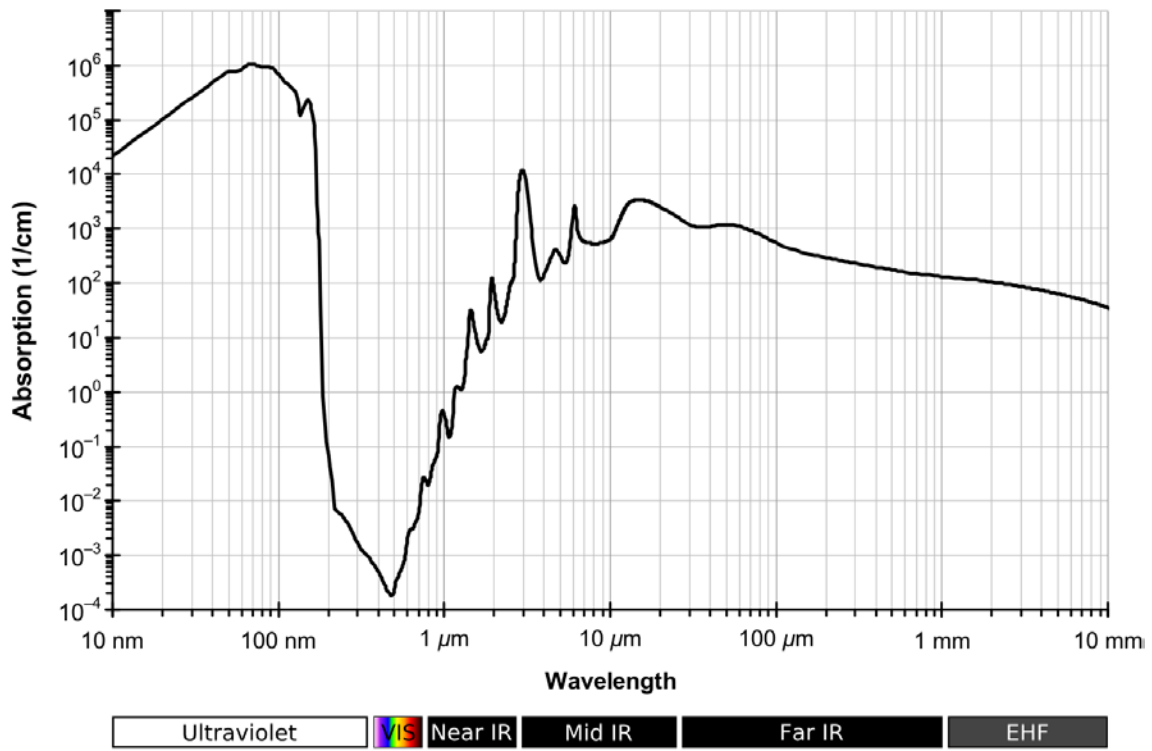
FIGURE 4.3 Absorption spectrum for water [44].

Figure 4.3 also illustrates the increase in water absorption as the wavelength of
the radiation increases from 525 nm to approximately 2941 nm (2.941 μm), where the
absorption coefficient is approximately 17,700 cm^{-1} [16]. This means EM radiation with
a wavelength of 2.941 μm has an absorption coefficient of approximately $1.5x10^7$ times
greater than the absorption coefficient for 525 nm in water. This trend is extremely
relevant to quantifying the amount of radiant energy for any given wavelength
(particularly in the visible and NIR) at any given point along its path within a water
medium.

The eye has its own absorption spectrum. Shown in Figure 4.4 is the ocular

transmission for visible and NIR radiation with wavelengths ranging from 300 nm to

approximately 1500 nm through various layers of the eye beginning with the cornea.
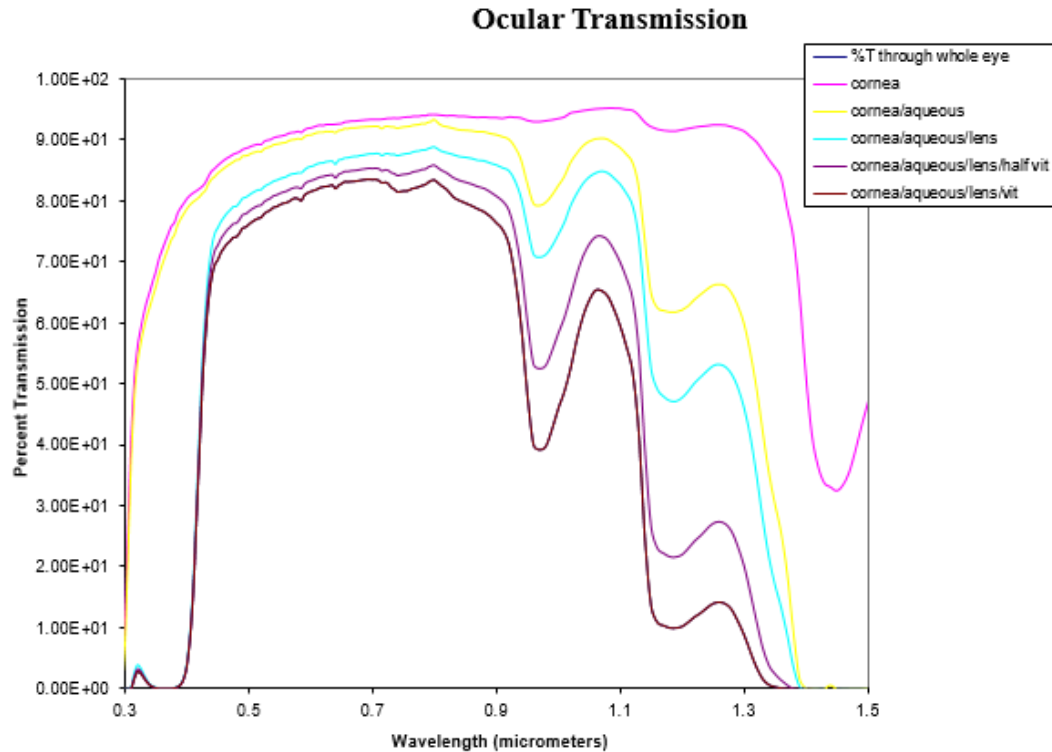
FIGURE 4.4 Ocular transmission through various layers of the eye. Picture taken from
Maher [16].

From the figure, we observe that the percentage of transmission decreases as more layers

of the eye are considered. The cornea, for example, allows a higher percentage of

transmission at any given wavelength (within the wavelength range specified in Figure

4.4) than the cornea-aqueous-lens combination. The percentage of transmission to the

retina is lowest when we consider all optical components of the eye, which include the

cornea, aqueous humor, lens, and the vitreous humor. While there still is some amount

of absorption taking place in the aqueous humor and lens shown by the drop in

transmission curves, especially in the 1150 nm to 1400 nm range, the amount of

absorption pales in comparison when we include the vitreous humor, which is indicative

by the large drops in transmission curves in the 1150 to 1400 nm wavelength range.

This means that any radiant energy making it past the lens will be highly absorbed in the

vitreous humor (especially in the 1200 nm to 1400 nm wavelength range), resulting in a

much smaller amount of radiant energy reaching the retina.

CHAPTER V

RADIANT ENERGY, RADIANT EXPOSURE, AND THE BEER-LAMBERT-

BOUGUER LAW

5.1 RADIANT ENERGY AND RADIANT EXPOSURE

When a beam of light passes through a positive, convex lens, the beam of light

will converge to a tightly concentrated spot, where the amount of radiant energy is

contained in the smallest area than the rest of the beam path. This spot, where the

energy per cross sectional area is maximized, is known as the focus. As the beam

propagates beyond the focal point, the beam begins to diverge, which means that the

radiant energy begins to distribute itself over a larger cross sectional area of the beam.

The radiant energy, measured in Joules (J), which is distributed over an amount of area,

measured in square-centimeters (cm^2), is defined as the radiant exposure, H, and is given

by the following equation:

$$H = \frac{Q}{A} = \frac{Q}{\pi r^2} \tag{5.1}$$

The variable Q represents the radiant energy distributed while r represents the radius of

the cross sectional area of the beam, assuming a circular cross sectional area. Therefore,

as the cross sectional area of the beam decreases and the beam propagates closer to its

focus, the radiant exposure, H, increases assuming the radiant energy of the beam

remains constant throughout the cross sectional area. As radiant energy from a light

source propagates through a medium, however, such as water, blood, oil, or the earth's

atmosphere, the radiant energy of that light source gets attenuated via absorption and

scattering by the medium as the radiant energy interacts with the particles that compose the medium.

5.2   THE BEER-LAMBERT-BOUGUER LAW

The absorption discussed in section 5.1 occurs in accordance with the Beer-Lambert-Bouguer Law, which is given by the following equation:

$$H(x) = H_0 e^{-\beta_a x} \tag{5.2}$$

The Beer-Lambert-Bouguer Law (Equation 5.2) illustrates that the two parameters involved in reducing the amount of incident electromagnetic radiant exposure, H_0, due to absorption are the absorption coefficient, β_a, which quantifies the amount of absorption per incremental path length of the medium, as well as the total path length, x, that the electromagnetic radiation propagates within the medium. In addition, the amount of absorption within the medium depends on the wavelength of electromagnetic radiation that is interacting with the medium (see section 4.2). For the purpose of this research, the absorption spectrum for water shown in Figure 4.3 in the 400 to 1600 nm range (i.e. 0.4 to 1.6 µm) illustrates a wide range in absorption coefficient depending on the wavelength of the EM radiation. For visible light approximately 480 nm in wavelength, the absorption coefficient takes on a significantly low value of approximately 0.0001 per cm. Therefore, for example, given an initial radiant exposure of 10 J cm^{-2} and assuming negligible absorption from the cornea-lens system, and propagating over a distance of 2.4 cm (the approximate length of the vitreous humor), a 480 nm beam will have a final radiant exposure of 9.964 J cm^{-2} at the retina. Relatively speaking, this represents a 0.36

28

per cent decrease. However, for NIR radiation at approximately 1350 nm, the absorption coefficient takes on a value of approximately 3.48 cm^{-1}, a factor of approximately 2,320 times greater than that of the absorption coefficient at 480 nm.

Considering the same initial radiant exposure of 10 J cm^{-2} entering the eye and again propagating through the vitreous humor over a distance of 2.4 cm, the NIR radiation with wavelength of 1350 nm will have a final radiant exposure at the retina of 2.359 mJ cm^{-2}, corresponding to a 99.99 per cent decrease in radiant exposure. It is clear that the dependence on wavelength of the absorption coefficient plays a significant role with the amount of radiant energy reaching a target. The percent of transmitted radiant energy decreases significantly with increasing wavelength of propagated electromagnetic radiation within the 400 nm to 1600 nm range as well as increasing propagated path length within the medium. Notice that in the calculated radiant exposures listed in Table 5.1, the absorption coefficients for water were used instead of those listed for the vitreous humor. This is primarily because the experiment, which will be described in a later chapter, utilized water and not an eye *in vivo*. The absorption coefficients for distilled water and the vitreous humor are listed simultaneously in Figure 5.1 to indicate the relative similarities in value, allowing for the validity in applying the results in distilled water to that of the eye and the vitreous humor.

The eye, however, does not transmit light to the retina in the 400 nm to 1400 nm wavelength range entering the pupil as a simple collimated beam shown in Figure 5.1. In fact, for that specific wavelength range shown in Figure 4.2 as visible and near-infrared, the cornea-lens system focuses electromagnetic radiation to a focus point on the

29

retina with a diameter of approximately 10 µm (i.e. radius of approximately 5 µm) over

a path length of approximately 2.4 cm as shown in Figure 5.2 [15].
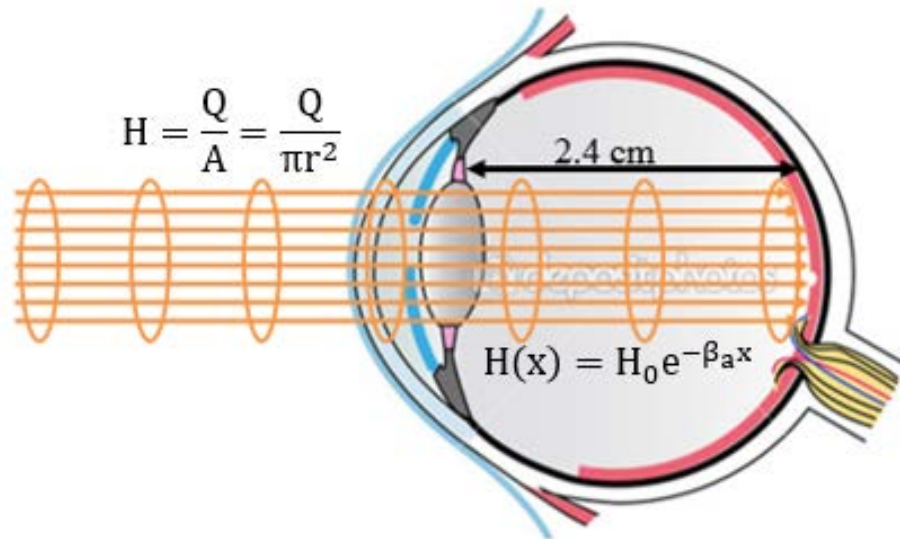
FIGURE 5.1 Schematic of the eye with a beam of visible/NIR radiation without
focusing by the cornea-lens system [45].

Since the index of refraction in the vitreous humor has a value approximately

equal to that of water (n=1.333), and since the electromagnetic radiation with

wavelengths ranging between 400 nm and 1400 nm is focused by the cornea-lens

system, the radiant energy reaching the retina can still be approximated knowing the

radiant energy entering the cornea-lens system using the Beer-Lambert-Bouguer Law in

the previous example. The difference now, however, is that the radiant energy is being

focused by the cornea-lens system while experiencing absorption simultaneously.

λ (nm)	$\beta_\alpha(\text{cm}^{-1})$ Distilled Water	$\beta_\alpha(\text{cm}^{-1})$ Vit. Humor	H_0 (J cm^{-2})	$H(2.4\text{cm})$ (J cm^{-2})	% Increase
480	.0015	.0565	10	9.964	-0.36
1200	1.27	1.33	10	0.474537	-95.25
1300	1.38	1.42	10	0.364432	-96.36
1350	3.48	3.29	10	0.00235924	-99.99
1400	19.1	15.3	10	1.24×10^{-19}	~ -100

TABLE 5.1 Hypothetical radiant exposure calculations demonstrating the effect that absorption has on radiant energy via the Beer-Lambert-Bouguer Law, where the absorption coefficient depends on the wavelength of the propagating radiation.
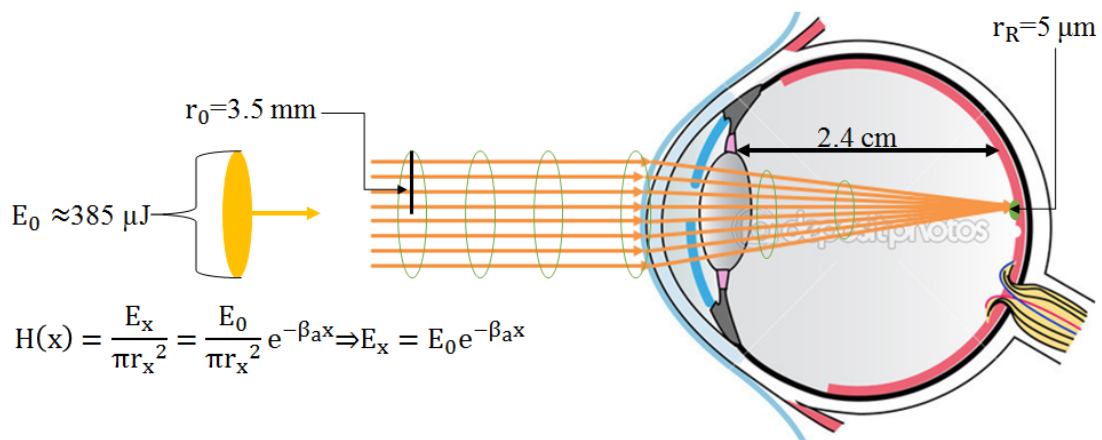
FIGURE 5.2 Schematic of the eye with a beam of visible/NIR radiation with focusing by the cornea-lens system [45].

The following equation gives the actual radiant exposure within the eye:

$$H(x) = \frac{E_x}{\pi r_x^2} = \frac{E_0}{\pi r_x^2} e^{-\beta_a x} \Rightarrow E_x = E_0 e^{-\beta_a x} \tag{5.3}$$

where E_x is now the radiant energy distributed in the cross sectional plane of the beam, r_x is the radius of the cross sectional beam at a distance x, and E_0 is the incident energy entering the eye. Since the maximum dilation of the human pupil is approximately 7

mm, approximating r_0 with a value of 3.5 mm provides the least conservative analysis in approximating the true amount of radiant energy entering the pupil of the eye. For example, an NIR beam with a wavelength of 1300 nm and an amount of incident radiant energy, E_0, approximately equal to 385 μJ entering the pupil (i.e. $r_0 = 3.5$ mm) will have a radiant exposure value of approximately 10 J cm^{-2}. While the beam propagates from the cornea-lens system to the retina, the beam will focus to a smaller radius while the energy of the beam gets absorbed by the vitreous humor. Assuming the beam gets absorbed in accordance with the Beer-Lambert-Bouguer Law and the absorption coefficient of the vitreous humor is similar to that of water at 1300 nm (i.e. $\beta_a = $ 1.38/cm), then the beam will reach the retina with a focused radius of 5 μm and radiant energy of approximately 14.031 μJ, corresponding to a radiant exposure of approximately 17.864 J cm^{-2}. There are a couple of relevant concerns that can are extrapolated from the above calculation. First, the radiant exposure has increased by approximately 79 percent at the retina than the point at which the beam entered the cornea-lens system in spite of the attenuation of the beam energy due to the absorption of the vitreous humor. Second, the shorter wavelength (higher frequency) electromagnetic radiation, within the 400 nm to 1400 nm range, gets absorbed less by the vitreous humor, which implies an increase in radiant exposure from the cornea-lens system to the retina by percentages greater than 79 percent for wavelengths shorter than 1300 nm.

Table 5.2 lists hypothetical radiant exposure calculations that demonstrate the effect that focusing has on radiant exposure. The focusing strength of the cornea-lens

system dramatically overcomes any losses in radiant energy due to absorption for

wavelengths less than or equal to 1300 nm.

λ (nm)	β_α(cm^{-1})	H_0(J cm^{-2})	H(2.4 cm) (J cm^{-2})	% Increase
480	.0015	10	488.436	4784.36
1200	1.27	10	23.262	132.62
1300	1.38	10	17.864	78.64
1350	3.48	10	0.116	-98.84
1400	19.1	10	6.058×10^{-18}	~ -100

TABLE 5.2 Hypothetical radiant exposure calculations demonstrating the effect that focusing has on radiant exposure.

CHAPTER VI

PEAK POWER, LASER SAFETY THRESHOLDS, MAXIMUM PERMISSIBLE

EXPOSURES (MPEs), RECENT ANSI CHANGES

6.1   PEAK POWER

When a pulse of EM radiation travels through space, the three critical

characteristics are the temporal shape of the pulse, the total pulse energy, and the pulse

width. Figure 6.1 shows two examples of possible temporal pulse shapes: Gaussian
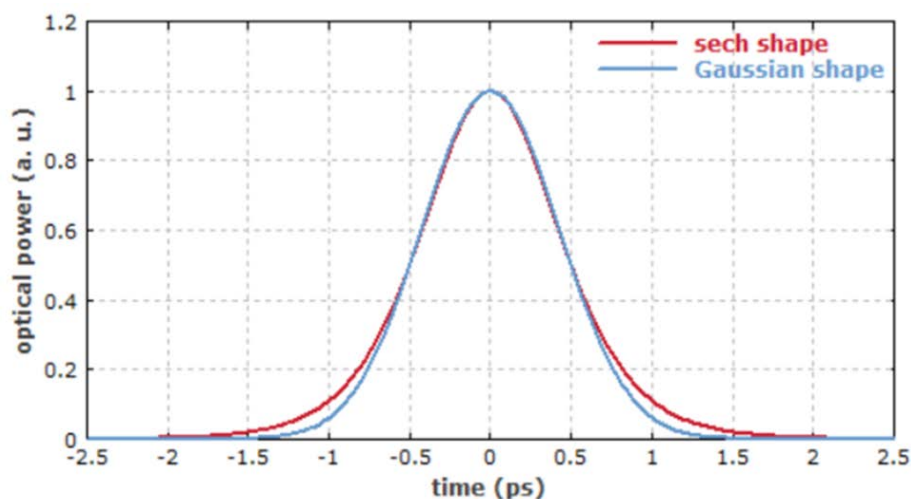
FIGURE 6.1 Temporal shape of Gaussian and hyperbolic secant (sech) pulses.

and hyperbolic secant. The pulse energy is the total area under the curve. If we assume

that the pulse width for the Gaussian shaped pulse in Figure 6.1 is 2 ps (pulse width

encompassing majority of the area under the curve), then the radiant energy of the pulse

will be the area under the curve between $t = {}^+/\!- 1$ ps. The peak power is the maximum

amplitude value of 1 a.u. (arbitrary units of optical power) in Figure 6.1. If the pulse

width were shortened to 1 ps, for example, and the energy per pulse remained constant,

then the area underneath the curve would remain constant over a shorter time interval,

implying that the maximum amplitude must be much higher than 1 a.u. and therefore

having a higher peak power. This means that peak powers increase by shortening the

pulse width in time while keeping the energy per pulse constant. The relationship

between peak power, energy per pulse, and pulse duration can best be expressed by the

following:

$$\text{Peak Power} = \frac{\text{Energy per Pulse}}{\text{Pulse Duration}} \tag{6.1}$$

6.2   LASER SAFETY THRESHOLDS AND MAXIMUM PERMISSIBLE

EXPOSURES

The *American National Standard for Safe Use of Lasers* 2014 Edition (ANSI

Z136.1-2014) has established laser safety thresholds to prevent damage to the different

optical components of the eye. The thresholds typically consider the amount of radiant

exposure, measured in J cm^{-2}, entering the cornea for EM radiation with wavelengths

ranging from the UV to the FIR. In addition, the thresholds place much consideration to

exposure durations as well. Figure 6.2 shows laser safety thresholds, maximum

permissible exposures (MPEs), from the 2007 ANSI standard. The threshold is lowest

for visible light having wavelengths ranging from 400 – 700 nm. The term maximum

permissible exposure (MPE) is given to indicate the maximum amount of radiant

exposure to the cornea of the eye before running the risk of possibly damaging any of the critical optical components of the eye.
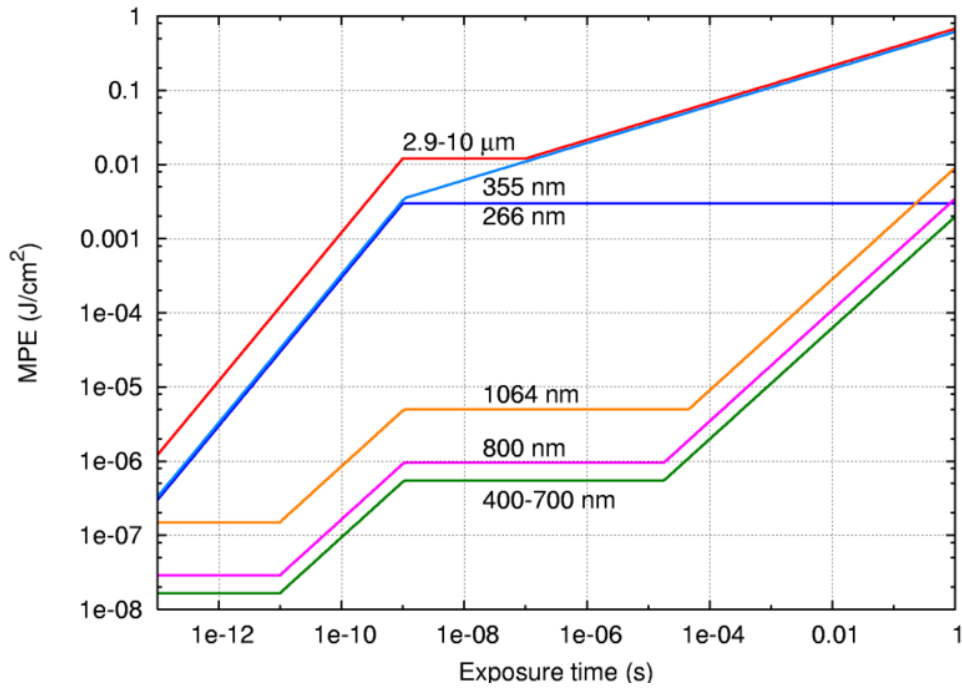
FIGURE 6.2 Laser safety thresholds [46].

Any radiant exposure amounts above the threshold curves shown in Figure 6.2 runs the risk of damage to the cornea, lens, or retina (see section 4.1). For EM radiation with wavelengths 266 nm, 355 nm, and ranging from 2.9 to 10 µm, the MPE thresholds are much higher than for the wavelengths 400 – 700 nm, 800 nm, and 1064 nm shown. This is very much due to the fact that UV and FIR radiation gets absorbed by the cornea-lens system and is highly attenuated when it reaches the retina, while the visible and NIR radiation reaches the retina without significant attenuation. Also, as the exposure time

36

becomes shorter (i.e. from nanoseconds to picoseconds), and assuming constant energy per pulse, the peak power becomes significantly higher (see Equation 6.1), resulting in lower MPE thresholds.

6.3   RECENT ANSI CHANGES

The most recent ANSI Edition is the 2014 version, which indicates a significant change for wavelengths in the 1300 nm to 1400 nm wavelength range with pulse durations of 100 fs as illustrated in Figure 6.3. The significant increase in MPEs in the NIR is justified based on minimum visible lesions (MVL) collected for nanosecond to seconds of exposure durations [6, 8]. The significant increase in pulse energy required to damage the retina as wavelength increases from 1200 nm to 1400 nm is due to the significant absorption in the anterior portions (i.e. vitreous humor) of the eye in this wavelength range. The data used in Figure 6.3 uses the assumption that MVLs will occur under similar conditions for femtosecond pulse durations as they did for nanosecond to second exposures. This assumption has not been tested via the observation of MVLs using femtosecond pulses. As a result of the significant linear absorption (low percent transmission shown in Figure 6.4), the radiant exposure required for a retinal lesion in this NIR regime is significant. While this trend should continue for picosecond and femtosecond pulse durations, there are also other nonlinear optical phenomena present which have not been considered.
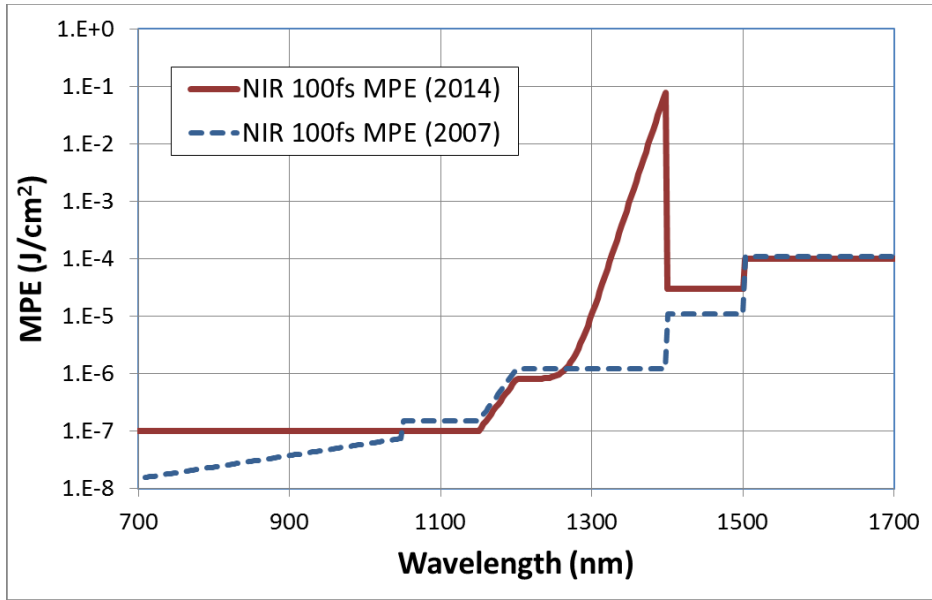
FIGURE 6.3 Laser safety threshold comparison of the most recent 2014 ANSI standard to the previous 2007 ANSI standard.
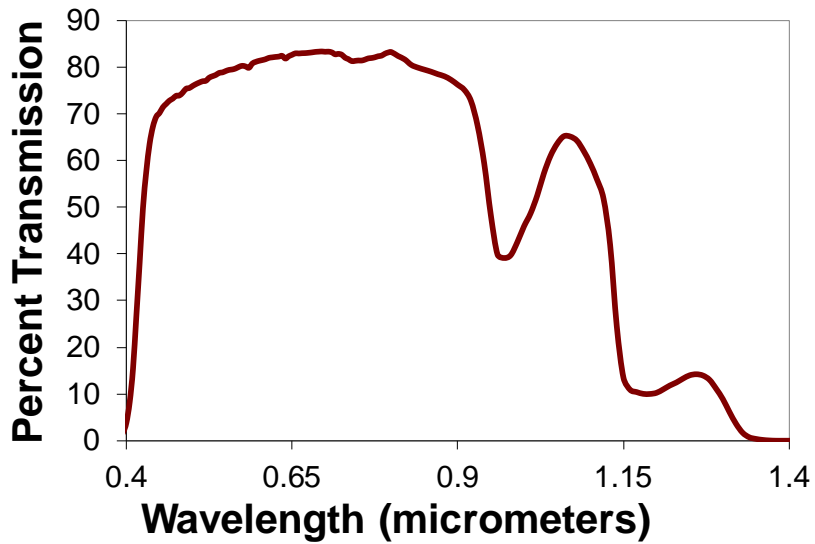
FIGURE 6.4 Percent transmission of the whole eye. Maher [16].

38

Previous research indicates that frequency broadening of laser pulses was first observed in self-focused filaments in the mid-1960s [33-36]. The generation of white light by laser radiation was first reported in 1970 by Alfano and Shapiro [38] using a picosecond second-harmonic output of a neodymium garnet laser with an energy of about 5 mJ in borosilicate glass [39]. Since June 1977, where superbroadening production was achieved in H_2O and D_2O by 30 ps and 21 ps pulses at 1.06 µm and 0.53 µm, respectively [37], few observations of SC generation have been reported for ultrashort pulses with wavelengths greater than 1000 nm (i.e. 1 µm), most of which have occurred for pump wavelengths of approximately 800 nm. In fact, the first account of SC generation with femtosecond laser pulses at 1300 nm and 1350 nm was reported in 2014 [40]. Due to the scarce research regarding SC generation for femtosecond pulsed lasers for NIR wavelengths ranging from 1200 nm to 1400 nm, considering nonlinear effects such as SC generation in laser safety thresholds is critical, especially since the production of NIR femtosecond pulsed laser systems is on the rise. This experiment will show that the SC nonlinear phenomenon can in fact be generated in water by any focused wavelength, particularly wavelengths in the 1200 nm to 1400 nm range. Once the beam is focused, nonlinear optical processes produce a super-broadened range of wavelengths ranging from 400 nm to 1400 nm. Our analysis will take into account the interplay between linear absorption through the thickness of the eye and the eventual radiant exposure that can be produced at the retinal plane.

CHAPTER VII

EXPERIMENTAL SETUP, PROCEDURE, AND BEAM CHARACTERIZATION

7.1   EXPERIMENTAL SETUP

The experimental setup took place at the Tri-Service Research Laboratory

located in Ft. Sam Houston, TX. Figure 7.1 shows a brief description of the

experimental setup. A non-collinear (femtosecond) optical parametric amplifier

(NOPA) was used to achieve the NIR radiation with tunable wavelengths ranging from

1150 nm to 1600 nm.
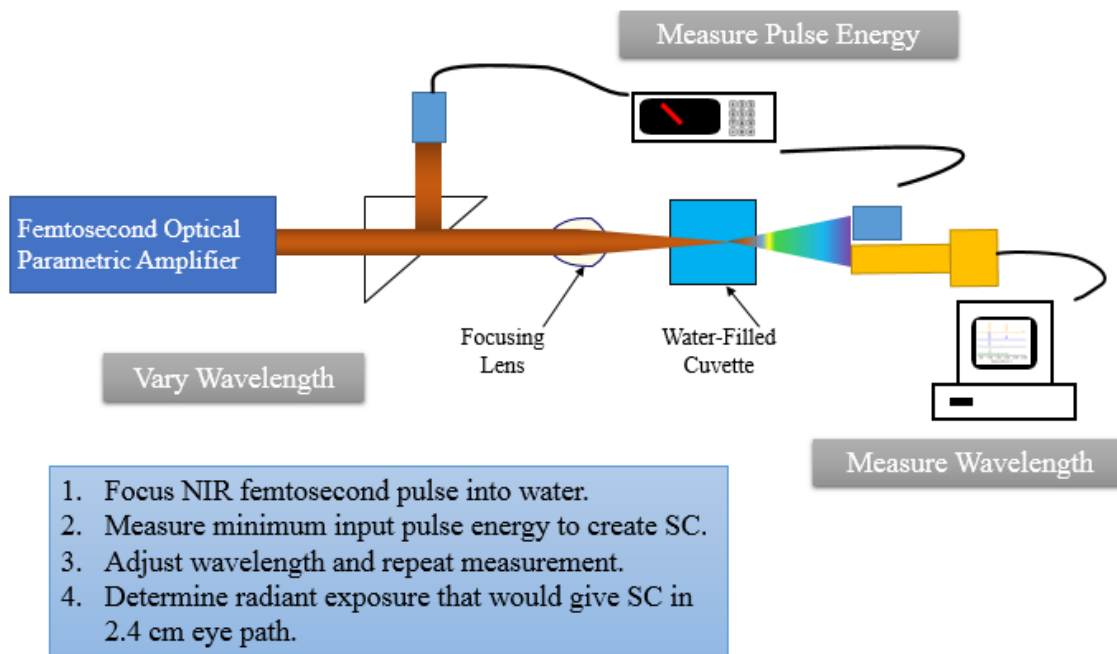
FIGURE 7.1 Experimental setup.

This NOPA was designed to generate ultrashort tunable pulses in this range [20]. For this experiment, this was accomplished using an 1 kHz Ti:Sapphire Regenerative Amplifier as the pump and seed source for the NOPA. The Regenerative Amplifier was centered at 805 nm with a 50 femtosecond pulse width and 1 mJ of radiant energy per pulse. Approximately 90% of the 805 nm beam was split off to pump the NOPA. This arm had a polarizing beam splitter cube and a half wave plate to control the pump energy. The other 10% of the 805 nm beam was used to generate a white light continuum in a quartz window. The pump beam was delayed to temporally overlap the white light continuum in the NOPA barium borate (BBO) nonlinear crystal. The BBO crystal was angle tuned to amplify the desired NIR frequency (i.e. wavelength).

7.2   PROCEDURE AND BEAM CHARACTERIZATION

As shown in Figure 7.1, a 1 kHz pulsed laser was fired through a 1 cm FUV Quartz glass cuvette, which was securely mounted on a translation stage. The dimensions of the glass cuvette are shown in Figure 7.2. Measurements were conducted with the cuvette empty and filled with distilled water. The pulsed laser was tuned to wavelengths ranging from 1150 nm to 1600 nm in increments of 50 nm. For each wavelength, the translation stage was positioned initially such that the focus of the laser beam was positioned at the front face of the glass cuvette, shown in Figure 7.2 as the left vertical wall. Caliper measurements revealed that the cuvette had a front thickness of 1.18 mm and a back thickness of 1.32 mm. The front and back walls were separated by a distance of 9.97 mm. Observations were recorded using two spectrometers; the first

ranging from 850 nm to 1740 nm (NIR) and the second ranging from 150 nm to 900 nm (UV-Visible-NIR).
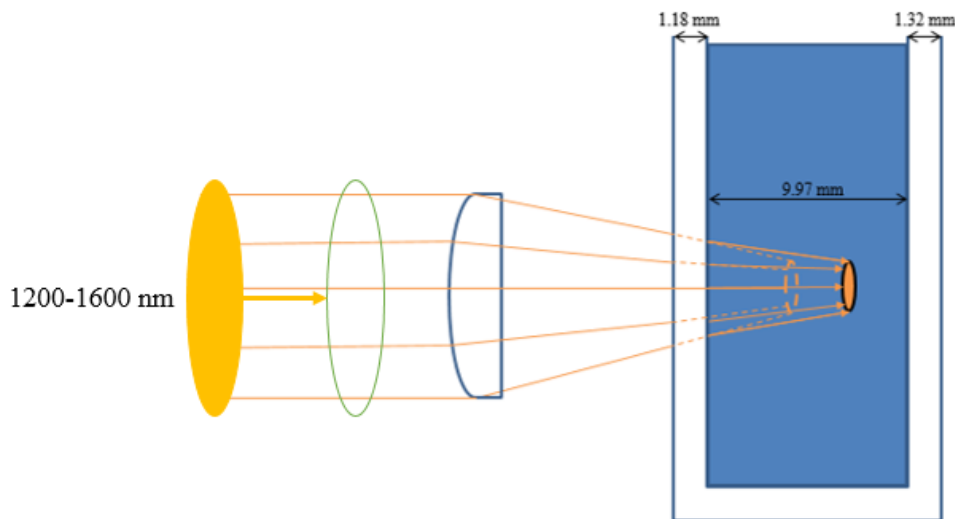
FIGURE 7.2 Cross sectional schematic drawing of laser beam entering the water-filled FUV Quartz cuvette.

Knowing the thickness of the glass, we initially verified that SC generation would in fact occur due to the thickness of the glass walls. We did this by pushing the focus of the beam through the front glass wall (cuvette empty) all the way through the back glass wall. We observed SC generation while the virtual focus was within the front and back walls. No SC generation was observed when the virtual focus was in the empty space between the walls of the cuvette. The term virtual is used here to indicate the position of the actual focus of the laser beam in air without any interaction with a medium. We call it virtual because of the fact that the actual focus is actually located deeper within the propagated medium (i.e. the glass or water) due to the change of index of refraction and Snell's Law, which will be discussed in greater detail in a later chapter.

In Figure 7.2, the virtual focus is indicated by the dashed focus disk, appearing closer to the front glass wall than the actual focus, which appears closer to the back wall of the cuvette.

The cuvette was then filled with distilled water and the process of generating SC was repeated starting with the focus of the beam at the front face of the glass cuvette. For wavelengths of 1450 nm, 1500 nm, 1550 nm, and 1600 nm, the SC generated within the water-filled cuvette coincided with SC generated at the front glass wall when the cuvette was empty. These observations lead to the inconclusiveness of SC generation due to the water or glass at those specific wavelengths. Interestingly enough, however, SC was not generated in the back glass wall when the cuvette was filled with distilled water, whereas SC was generated when the cuvette was empty. This is consistent with the notion that the focusing of the beam, thereby increasing the radiant exposure, does not overcome the rate of water absorption at those wavelengths (i.e. 1450 – 1600 nm); never reaching intensities high enough to drive the SPM nonlinear process for SC generation. Recalling that IR radiation with wavelengths greater than 1400 nm is highly absorbed by the cornea (see section 4.1) and therefore does not get focused to the retina, the inability to determine whether or not the SC generated was due to the glass walls of the cuvette or the water inside the cuvette seemed irrelevant to the purpose of the experiment.

For the radiation with wavelengths 1200 nm, 1250 nm, 1300 nm, 1350 nm, and 1400 nm, SC generation due to the distilled water was observed over a range (distance in mm) inside the water cuvette. The range indicated the position of the virtual focus

where SC was generated. Within that range was a single position where the SC

generation was maximum as observed on the spectrometer. After determining the

position of maximum SC generation, the input energy per pulse was decreased to SC

generation threshold (i.e. the minimum input energy required to generate SC). The

process was repeated for each of the specified tunable wavelengths. The data was used

to approximate radiant exposures that would generate SC in a 2.4 cm eye path length,

which will be shown in a later chapter.

Knife Edge Technique
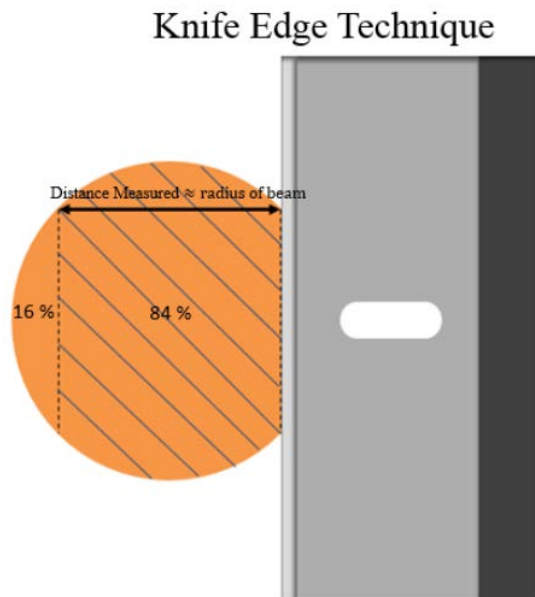
FIGURE 7.3 The knife edge technique. Cross sectional schematic drawing of the laser
beam clipped by a razor blade.

Beam radius is measured by measuring the distance a sharp edge blade moves in

blocking 16 percent to 84 percent of the beam intensity. This knife-edge technique,

shown in Figure 7.3, was used to characterize the tunable 1150 nm to 1600 nm laser

beam before the glass cuvette configuration. Using this technique, the radius of the

collimated beam entering the sample lens was measured at 3.177 mm. The knife-edge

technique was used to determine the beam radius before the first data set and

immediately after the last data set taken during this experiment. A Galilean telescope

was inserted into the beam path in order to achieve collimation and reduce beam

divergence entering the sample lens which initially had a divergence angle of several

milliradians without the Galilean telescope. Using the equation for a two thin lens

combination [21], an appropriate configuration was determined for the Galilean lens

system:

$$\frac{1}{f_{eff}} = \frac{1}{f_1} + \frac{1}{f_2} - \frac{d}{f_1 f_2}$$

(7.1)

where f_{eff} is the effective focal length of the system, f_1 and f_2 are the focal lengths of the

individual thin lenses, and d is the distance between the two thin lenses within the

telescope system. The use of the Galilean telescope in our beam path resulted in a beam

divergence of 0.5 mrad, which resulted in a spot size of approximately twice the

diffraction limit (best resolution) of the system at 1300 nm. The diffraction limit was

calculated using a lens with a much longer focal length of 513 mm at the 1300 nm

wavelength than was used in the quartz glass experiment. The limit of resolution

equation (Equation 7.2 below) [22] yielded a value of approximately 127 µm, where λ

was equal to 1300 nm, f was equal to 513 mm, and the diameter of the beam at the

aperture was equal to 6.36 mm.

$$\text{Diffraction Limit} = \frac{1.22 * \lambda * f}{D}$$

(7.2)

This meant that the measured focus diameter of 284.5 µm (using the 513 mm focal length lens) was a little over twice the diffraction limit value, which led to a divergence half angle of 0.5 mrad. The knife edge technique was chosen due to the geometry of the focused beam, which prior research has shown to provide an excellent characterization of focusing quality [23]. Figure 7.4 illustrates the two lenses used in this experiment. The first lens (Thor Labs Lens KPX 118) has a focal length of 513 mm at wavelength 1300 nm and was used to determine the divergence angle of the collimated beam using the following equation shown in Figure 7.4:

$$\theta_{half} = \frac{r_0}{f} \tag{7.3}$$

where r_0 was measured at 284.5 µm using the knife-edge technique and the focal length, f, was specified at 1300 nm for the KPX 118 lens. The second lens (Thor Labs Lens 1131C) was used to focus the laser beam in the quartz glass cuvette. Using Equation 7.3, we were able to estimate the radius of the focus, r_0, in air for the 1131C lens. Since the focal length is wavelength dependent, the radius of the focus is also wavelength dependent by using Equation 7.3. A 513 mm focal length lens at wavelength 1300 nm was used to estimate the divergence half-angle of the collimated beam. Once established, the half-angle is used in estimating the radius of the focus for the 51.2 mm focal length lens at wavelength 1300 nm. The values for the wavelength-dependent focal lengths and focus radii for the 1131C lens are shown in Figure 7.4. The pulse width was measured at 35 fs ($^+/_-$ 5 fs) using an autocorrelator.

Pulse Width $\tau \approx 35$ fs +/− 5 fs

$r_0 = \theta_{half} * f(1300\,nm) \implies \theta_{half} = \frac{r_0}{f} = \frac{284.5\,\mu m}{513\,mm} \approx \boxed{0.5\,mrad}$

f(1300 nm) = 513 mm

θ_{half}

Thor Labs Lens KPX 118

$r_0 = \theta_{half} * f \implies r_0 = \theta_{half} * f = 0.5\,mrad * f(\lambda)$

θ_{half}

f(1300 nm) = 51.2 mm

Thor Labs Lens 1131C

λ (nm)	f(λ) (mm)	Focus Radius r_0 (μm)
1200	51.1	25.6
1250	51.2	25.6
1300	51.2	25.6
1350	51.3	25.7
1400	51.3	25.7
1450	51.4	25.7
1500	51.4	25.7
1550	51.5	25.8
1600	51.5	25.8
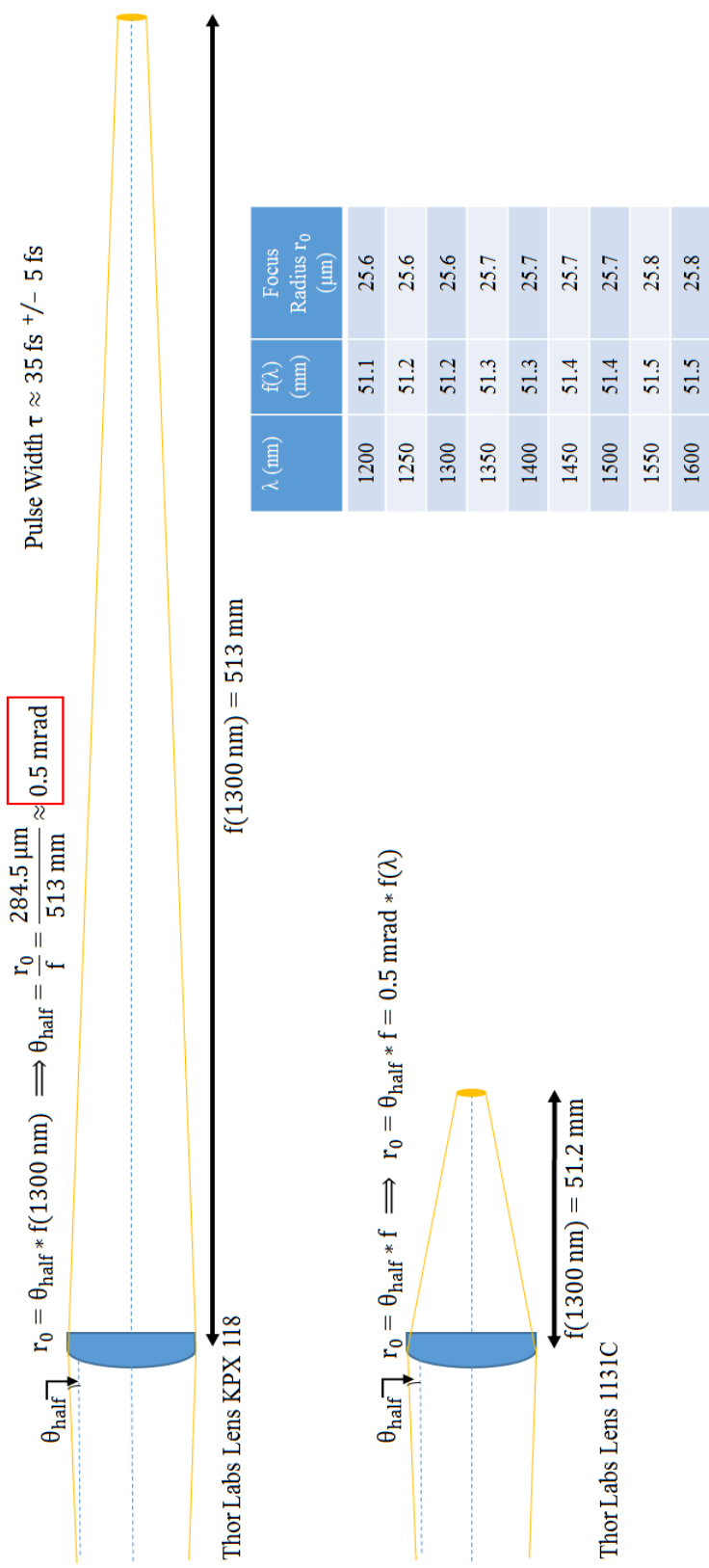
FIGURE 7.4 Beam characterization.

CHAPTER VIII

WATER CUVETTE EXPERIMENT: ESTABLISHING ABSORPTION PATH

LENGTH IN WATER MEDIUM, EXPERIMENTAL MEASUREMENTS AND

RESULTS

8.1 ESTABLISHING ABSORPTION PATH LENGTH IN WATER MEDIUM

As previously discussed in sections 5.2 and 6.3, there is an interchange occurring

as a pulse of EM radiation gets focused within a medium. To understand more

completely the exchange between water absorption and radiation exposure, we need first

to calculate a path length for which the NIR beam will experience absorption from the

distilled water in the glass cuvette. Since the SC generation nonlinear effect is highly

dependent on the laser beam achieving intensities high enough to drive the SPM process,

it is most critical to establish where along the water path the NIR beam will reach its

maximum intensity. As mentioned earlier in section 5.1, any focused beam will

converge to a focus with the smallest cross sectional area before diverging. Since the

laser beam will continue to lose energy due to water absorption throughout the entire

propagated distance in the water (i.e. before and after the actual focus within the water),

then it logically follows that the portion of the water path that is most critical to

achieving maximum beam intensity, and maximum radiant exposure measured in radiant

energy per unit area, is from the point where the beam enters the water to the actual

focus within the water, before the beam begins to diverge. A schematic drawing of the

path length, γ, from the virtual focus point of entry of water cuvette to the actual focus

within the water is shown in Figure 8.1. The figure shows the mathematical relationship between the focused laser beam from the 50 mm (wavelength dependent) focusing lens in air to the water cuvette, and the point of entry of water cuvette to the actual focus within the water. Establishing this relationship was necessary based on the experimentally measured parameters for this study. Beginning with the far-field equation for a focused laser beam in air:

$$D_a^2(x) = a_0^2 + [(f - x)\varphi_{air}]^2 \tag{8.1}$$

where $D_a(x)$ is the diameter of the beam in air along some distance, x, from the focusing lens, a_0 is the focus diameter of the beam in air shown in Figure 8.1 as the virtual focus, f is the wavelength-dependent focal length of the lens in air, and φ_{air} is the full divergence angle of the laser beam in air. With regard to our experiment, $\varphi_{air} = 2 * \theta_{air}$. Experimentally, we were able to "push" the virtual focus into the water cuvette by actually moving the water cuvette from right to left, shown in Figure 8.1 as x'. In the figure, we can see that by moving the cuvette some distance, x', the distance from the 50 mm focusing lens to the cuvette will be given by subtracting the translation distance, x', from the focal length of the lens in air, or $f - x'$. The value for $f - x'$ is important because substituting that value for x in Equation 8.1 will give the following:

$$D_a^2(f - x') = a_0^2 + [(f - (f - x'))\varphi_{air}]^2 = a_0^2 + [x' * \varphi_{air}]^2 \tag{8.2}$$

which gives the diameter of the beam, and therefore allows for the calculation of the cross sectional area of the beam at the point of entry to the glass cuvette. Similarly, within the water cuvette, the far-field equation for a focused laser beam can be used.
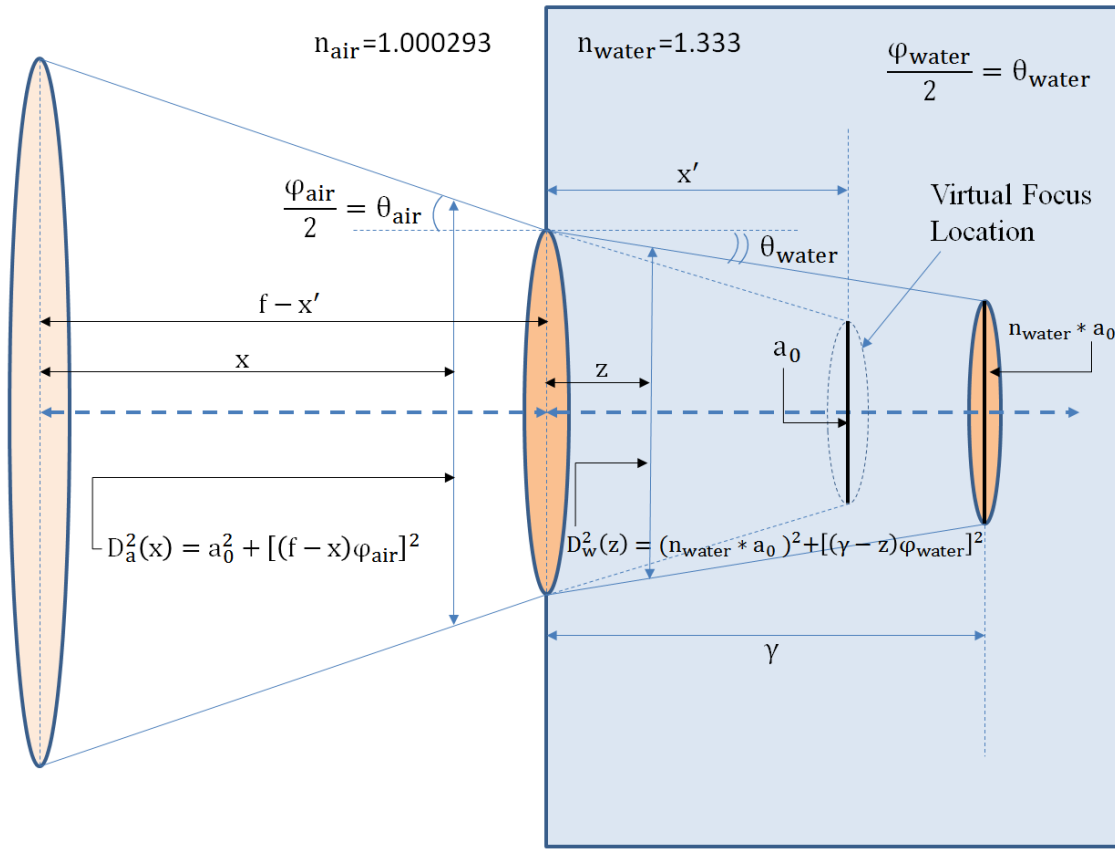
FIGURE 8.1 Calculating critical path length, γ, within water cuvette.

For this situation we define the focal length as γ, which happens to be the same parameter as the critical distance used in establishing the maximum intensity achieved by calculating the amount of radiant energy due to water absorption using the Beer-Lambert-Bouguer Law (see Equation 5.3). The far-field equation for the focused beam inside the water cuvette is as follows:

$$D_w^2(z) = (n_{water} * a_0)^2 + [(\gamma - z)\varphi_{water}]^2 \qquad (8.3)$$

where $D_w(z)$ is the diameter of the beam inside the water cuvette at some distance z from the front face of the water cuvette as shown in Figure 8.1. Knowing the values of

the parameter z is not particularly important, except for the fact that setting z equal to

zero allows Equation 8.3 to become:

$$D_w^2(0) = (n_{water} * a_0)^2 + [\gamma * \varphi_{water}]^2 \tag{8.3}$$

Observing that Equations 8.2 and 8.3 both yield the diameter of the beam at the point of

entry to the water cuvette, we get the following relationship:

$$D_a^2(f - x') = D_w^2(0) \implies a_0^2 + [x' * \varphi_{air}]^2 = (n_{water} * a_0)^2 + [\gamma * \varphi_{water}]^2 \tag{8.4}$$

Solving for γ gives

$$\gamma = \frac{\sqrt{a_0^2 + (x' * \varphi_{air})^2 - (n_{water} * a_0)^2}}{\varphi_{water}} \tag{8.5}$$

Recalling that $\varphi_{air} = 2 * \theta_{air}$, in water we get $\varphi_{water} = 2 * \theta_{water}$, where φ_{water} is the

full divergence angle of the laser beam within the water cuvette. Since θ_{air} is our

measured parameter, it is convenient to put all angles in terms of θ_{air}. Using Snell's

Law, we get the following:

$$n_{air} \sin \theta_{air} = n_{water} \sin \theta_{water} \tag{8.6}$$

Solving for θ_{water}, we get:

$$\theta_{water} = \sin^{-1}\left[\frac{n_{air}}{n_{water}} \sin \theta_{air}\right] \tag{8.7}$$

By substituting Equation 8.7 in $\varphi_{water} = 2 * \theta_{water}$ and then substituting into Equation

8.5, we arrive at the following equation:

$$\gamma = \frac{\sqrt{a_0^2 + (2x' \theta_{air})^2 - (n_{water} * a_0)^2}}{2 * \sin^{-1}\left[\frac{n_{air}}{n_{water}} \sin \theta_{air}\right]} \tag{8.8}$$

For simplification, let's assume that the diameter of the beam at the focus in water will be the same as the diameter of the beam at the focus in air (i.e. a_0). With this assumption, Equation 8.8 becomes:

$$\gamma = \frac{2x'\theta_{air}}{2*\sin^{-1}\left[\frac{n_{air}}{n_{water}}\sin\theta_{air}\right]} \tag{8.9}$$

It is important to indicate that the assumption of the beam diameter in water having the same value as the beam diameter in air is only for approximating the path length, γ, in water. In the following sections, we will consider both diameters (i.e. radii r_0 and $n_{water} * r_0$) when calculating the maximum radiant exposures at the focus.

8.2   EXPERIMENTAL MEASUREMENTS AND RESULTS

As mentioned earlier, the actual focal length of the 50 mm lens is wavelength dependent. In fact, 50 mm is the focal length of the lens for light passing through it with wavelength of approximately 600 nm. Table 8.1 lists the focal lengths, $f(\lambda)$, as a function of the NIR wavelength radiation passing through the lens. In addition, the radius of the focus, r_0, for each wavelength is also listed and was calculated by using Equation 7.3 (see section 7.2). Figure 8.2 illustrates the calculation of θ_{air}, the angle for which the laser beam is focused by the lens in air. Another way of calculating the focusing angle, θ_{air}, of the focused beam is to use the same far-field equation for a focused beam used in Equation 8.1 by setting x to zero. Using the equation

$$\tan\theta_{air} = \frac{3.177\text{mm}}{f(\lambda)\text{ mm}} \Longrightarrow \theta_{air} = \tan^{-1}\left(\frac{3.177\text{mm}}{f(\lambda)\text{ mm}}\right) \tag{8.10}$$

we can calculate the focusing angle, θ_{air}, for each NIR wavelength that is passed

λ (nm)	f(λ) (mm)	Focus Radius r_0 (µm)
1200	51.1	25.6
1250	51.2	25.6
1300	51.2	25.6
1350	51.3	25.7
1400	51.3	25.7
1450	51.4	25.7
1500	51.4	25.7
1550	51.5	25.8
1600	51.5	25.8

TABLE 8.1 List of focal lengths as they depend on the wavelength of NIR radiation passing through the lens.

$$\tan \theta_{air} = \frac{3.177\text{mm}}{f(\lambda)\ \text{mm}} \implies \theta_{air} = \tan^{-1}\left(\frac{3.177\text{mm}}{f(\lambda)\ \text{mm}}\right)$$
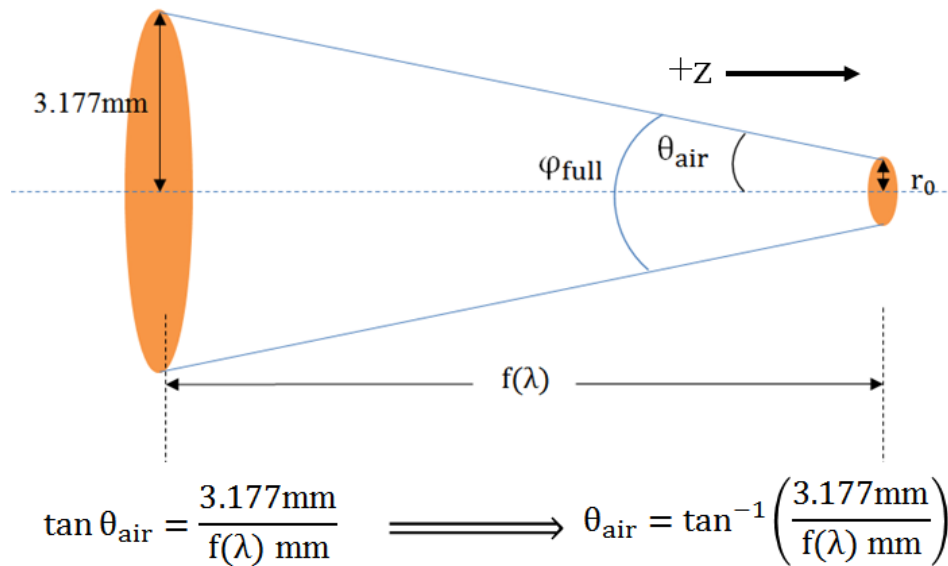
FIGURE 8.2 Calculating the focusing angle for the wavelength-dependent focusing lens. The radii of the beam at the lens (3.177 mm) and focus were measured using the knife-edge technique.

through the focusing lens, which will yield different values for the path length in water, γ, (Equation 8.9) used in calculating resultant radiant energy, E_γ, due to water absorption at the various wavelengths over γ. In addition, the range for which SC generation was observed is also shown in Table 8.2. The values for x' indicate the position of the virtual focus where the maximum SC was observed. Table 8.2 shows the calculated focusing angles, θ_{air}, for each wavelength. For each wavelength, the position of the actual focus (i.e. at the γ path length values listed in Table 8.2) was located deeper into the water cuvette.

λ (nm)	β_α (cm^{-1})	$f(\lambda)$ (mm)	θ_{air} (mrad)	Range of SC Generation Observed (mm)	x' @ Max SC Effect (mm)	γ path length in water cuvette (mm)
1200	1.27	51.1	62.1	1.265-12.573	5.837	7.781
1250	1.08	51.2	62.0	1.519-11.933	5.329	7.103
1300	1.38	51.2	62.0	0.503-12.573	5.456	7.273
1350	3.48	51.3	61.9	1.646-7.234	4.44	5.918
1400	19.1	51.3	61.9	0.757-11.933	5.583	7.442
1450	30.9	51.4	61.7	1.392-5.202	2.738	3.650
1500	19.8	51.4	61.7	0.884-3.932	2.408	3.210
1550	11.2	51.5	61.6	0.884-4.186	1.773	2.363
1600	7.36	51.5	61.6	1.138-4.440	1.900	2.533

TABLE 8.2 Observations of SC generation within the water filed cuvette.

Notice that for wavelengths 1450 nm, 1500 nm, 1550 nm, and 1600 nm, SC was observed at distances within or near the front glass wall of the cuvette. As discussed earlier in section 7.2, the data for these wavelengths led to the inability to determine whether the SC generated was due to the front glass wall of the cuvette or the water inside the cuvette. For wavelengths of 1200 nm, 1250 nm, 1300 nm, 1350 nm, and 1400 nm, SC was observed with the virtual focus well within the center of the water filled region in the glass cuvette. For these wavelengths, the actual focus was located past the center of the water region (i.e. approximately 5 mm), at positions of approximately 6 to 8 mm into the water filled glass cuvette. Table 8.3 shows the focused radii, r_0, in air for the NIR wavelengths. Shown are also the recorded minimum incident energies per pulse needed to generate SC at position x′, where the maximum SC was observed within the SC generation range.

λ (nm)	Focus Radius r_0 (μm)	Rayleigh Range for r_0 (mm)	Rayleigh Range for $1.333 * r_0$ (mm)	$r_{incident}$ (μm)	Minimum Incident Energy E_0 for SC Generation (μJ)
1200	25.6	1.716	3.049	363.4	0.158
1250	25.6	1.647	2.927	331.4	0.306
1300	25.6	1.584	2.814	339.2	0.578
1350	25.7	1.537	2.731	276.0	0.404
1400	25.7	1.482	2.634	346.5	1.956
1450	25.7	1.431	2.543	170.9	0.801
1500	25.7	1.383	2.458	150.8	0.250
1550	25.8	1.349	2.397	112.2	0.818
1600	25.8	1.307	2.322	119.9	0.978

TABLE 8.3 Focus radii and Rayleigh ranges for NIR wavelengths.

In addition, the radius of the beam at the point of entry to the glass cuvette, $r_{incident}$, is given for each wavelength and was calculated by using Equation 8.2 to get the following:

$$r_{incident} = \frac{D_a(f-x')}{2} = \frac{\sqrt{a_0^2 + [2*x'*\theta_{air}]^2}}{2}$$ (8.11)

The radius, $r_{incident}$, is necessary for calculating the incident radiant exposure at the entry point of the glass cuvette. Table 8.3 gives the minimum incident energy, E_0, per pulse needed to generate SC for each wavelength. This was done by locating the position of the virtual focus where the SC generated was maximum. Upon establishing the virtual focus position of maximum observed SC (i.e. at x'), the energy per pulse was reduced until the SC generated was no longer observed. Lastly, Table 8.3 shows the calculated Rayleigh ranges for each wavelength, which is defined for each focus radius within the water cuvette. Figure 8.3 illustrates the definition of the Rayleigh range z_R. The significance of z_R is that it represents a distance perpendicular to the cross section of the laser beam where the cross sectional area at z_R is exactly twice the cross sectional area at the focus with radius r_0. The Rayleigh range is often a useful parameter to know because it also represents the portion of the laser beam that is most intense. The Rayleigh ranges in Table 8.3 are likely useful in providing an explanation (or even prediction) of the range of SC generation observed shown in Table 8.2, perhaps when intensity is greatest due to focusing. In Figure 8.3, the parameter $b = 2 * z_R$ is shown. When enough of the Rayleigh range, or some factor involving the Rayleigh range, is

within the water medium (or any other nonlinear medium), intensities are able to

overcome the water absorption in order to achieve SC generation.

Rayleigh Range

FIGURE 8.3 Rayleigh range. The Rayleigh range, shown as z_R in the figure, is the distance away from the focus such that the cross sectional area is precisely twice the cross sectional area at the focus itself.

After establishing the path length in water, γ, the minimum incident energy per

pulse for SC observation, E_0, and the radius of the laser beam at the entry point of the

cuvette, $r_{incident}$, we are now able to calculate the minimum incident radiant exposures

for SC generation in the water cuvette using Equation 5.1, where E_0 represents the

radiant energy entering the water cuvette instead of the variable Q. Using Equation 5.3

from section 5.2 (see Beer-Lambert-Bouguer Law):

$$H(\gamma) = \frac{E_0}{\pi r_\gamma{}^2} e^{-\beta_a \gamma} \Rightarrow E_\gamma = E_0 e^{-\beta_a \gamma} \qquad (8.12)$$

we are also able to calculate the maximum radiant exposure achieved at the focus within

the water cuvette. Equation 8.12 uses r_γ, which is the radius of the beam at the focus

λ (nm)	Minimum Incident Radiant Exposure H_0 for SC Generation (μJ cm^{-2})	Focus Radius r_0 (μm)	Maximum Radiant Exposure H achieved in the water cuvette (i.e. Threshold at the focus spot inside the water) (mJ cm^{-2})	Focus Radius 1.333*r_0 (μm)	Maximum Radiant Exposure H achieved in the water cuvette (i.e. Threshold at the focus spot inside the water) (mJ cm^{-2})
1200	38.084	25.6	2.857	34.1	1.610
1250	88.688	25.6	6.901	34.1	3.890
1300	159.907	25.6	10.290	34.1	5.799
1350	168.816	25.7	2.483	34.3	1.394
1400	518.576	25.7	6.327×10^{-5}	34.3	3.552×10^{-5}
1450	872.968	25.7	4.880×10^{-4}	34.3	2.740×10^{-4}
1500	349.935	25.7	2.092×10^{-2}	34.3	1.175×10^{-2}
1550	2068.32	25.8	2.773	34.4	1.560
1600	2165.46	25.8	7.245	34.4	4.078

TABLE 8.4 Minimum incident radiant exposures for SC generation. Also included are the maximum radiant exposures achieved for the two possible focus radii, r_0 and 1.333 r_0 (i.e. $n_{water} * r_0$), within the water cuvette.

(i.e. at path length equal to γ), which takes on the values of r_0 and $n_{water} * r_0$. Table 8.4

also lists the minimum radiant exposures for each wavelength for SC generation

calculated by the following:

$$H_0 = \frac{E_0}{\pi r_{incident}{}^2} \qquad (8.13)$$

where E_0 is the measured minimum incident radiant energy for SC generation listed in

Table 8.3. The maximum radiant exposures calculated in Table 8.4 allows for the

comparison of foci with the two assumed radii, r_0 and $n_{water} * r_0$, mentioned previously

at the end of section 8.1. These values might be of particular interest if we assume that

these maximum radiant exposures achieved at the focus are used to estimate "minimum" intensities necessary for driving the SPM process to generate SC. By understanding that the minimum incident radiant exposures for observations of SC generation lead to minimum intensities (calculated with radiant exposure and pulse width) that drive the SPM process required for SC generation, we can begin to extend our analysis to the eye to determine the intensities that might be achieved within the vitreous humor that could lead to potential generation of white light (higher energy photons) being focused at the retina. It is important to note that we are now establishing thresholds in terms of radiant exposures achieved at the focus for pulse widths in the 30 to 40 fs range. It is equally important to note that these thresholds, which have not been well established in the scientific community, are specific to the parameters and materials within this study.

Using the data and calculations for the water cuvette experiment, we can extend the analysis using the configuration for the eye shown in Figure 8.4. Using the minimum incident radiant energy for SC generation measured in Table 8.3, the minimum incident radiant exposures are calculated for the eye and listed in Table 8.5. The table shows the values of the minimum incident radiant exposures entering the pupil for an eye with path length of 2.4 cm that is focused on the retina with a spot size radius of 5 µm. Maximum radiant exposures are calculated for the eye at the retina and compared to the thresholds listed from Table 8.4.

$$H(\gamma) = \frac{E_0 * e^{-\beta_a \gamma}}{\pi r_{focus}^2}$$
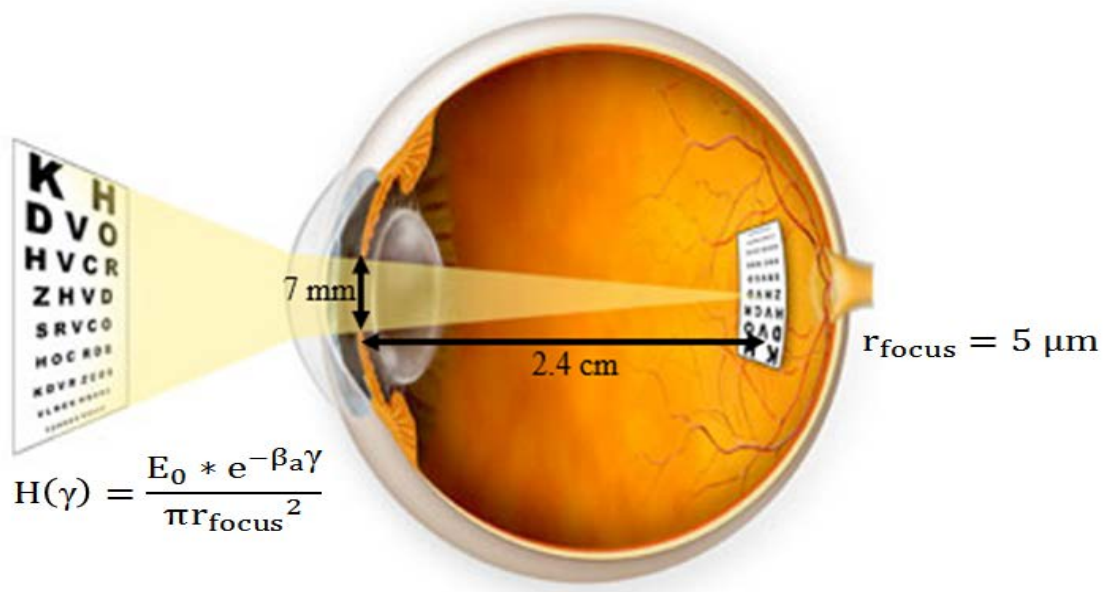
FIGURE 8.4 Diagram of the eye illustrating incident radiant energy focused on the retina, approximately 2.4 cm away from the lens [47].

λ (nm)	$r_{incident}$ (mm)	Minimum Incident Radiant Exposure H_0 for SC Generation (μJ cm^{-2})	Maximum Radiant Exposure H achieved at the retina	Maximum Radiant Exposure H achieved in the water cuvette (i.e. Threshold at the focus spot inside the water) (mJ cm^{-2})	Maximum Radiant Exposure H achieved in the water cuvette (i.e. Threshold at the focus spot inside the water)
1200	3.5	0.411	9.546 mJ cm^{-2}	2.857	1.610 mJ cm^{-2}
1250	3.5	0.795	29.170 mJ cm^{-2}	6.901	3.890 mJ cm^{-2}
1300	3.5	1.502	26.820 mJ cm^{-2}	10.290	5.799 mJ cm^{-2}
1350	3.5	1.050	121.357 μJ cm^{-2}	2.483	1.394 mJ cm^{-2}
1400	3.5	5.083	3.078x10^{-14} μJ cm^{-2}	6.327x10^{-5}	3.552x10^{-2} μJ cm^{-2}

TABLE 8.5 SC generation thresholds.

The diameter of the pupil is 7 mm (i.e. $r_{incident}$ = 3.5 mm), which is the size of diameter at maximum eye dilation. Using Equation 8.13, the minimum incident radiant

exposures are calculated using $r_{incident} = 3.5$ mm and the minimum incident radiant

energies, E_0, measured in Table 8.3. Using Equation 8.12, the maximum radiant

exposures achieved at the retina are also shown in Table 8.5. Comparing these values to

the radiant exposure thresholds (for 30 to 40 fs pulse widths) for the water cuvette

experiment, we see that the radiant exposures achieved at the retina exceed the

thresholds achieved at the focus for minimum SC observation in the glass cuvette

configuration for the 1200 nm, 1250 nm, and 1300 nm wavelengths regardless of which

focus radius is used in the water cuvette radiant exposure threshold calculations. For

NIR wavelengths of 1350 nm and 1400 nm, the maximum radiant exposures calculated

at the retina using the minimum incident radiant exposures for observed SC are less than

the radiant exposure thresholds in the water cuvette shown in Table 8.5. This

comparison for the 1350 nm and 1400 nm wavelengths is consistent with the increased

amounts of absorption, and over an increased distance of 2.4 cm in the vitreous humor,

which has an absorption coefficient similar to that of distilled water. This might indicate

that for focus intensities achieved for minimum SC generation in the water cuvette, the

extension of analysis to the eye configuration shows that intensities will not be achieved

for SC generation at the retina at NIR wavelengths of 1350 nm and 1400 nm. This will

be addressed in the following chapter.

CHAPTER IX

EXPERIMENTAL ANALYSIS VERSUS ANSI STANDARD, EMISSION

SPECTRUMS, AND ESTIMATING WHITE LIGHT RADIANT EXPOSURES

9.1   EXPERIMENTAL ANALYSIS VERSUS ANSI STANDARD

As mentioned at the beginning of this study, the purpose of conducting the water cuvette SC generation experiment was to extend the analysis of results to the eye configuration in order to emphasize the importance of considering nonlinear phenomenon, such as SC generation driven by nonlinear processes (e.g. SPM), in establishing lower MPE thresholds for picosecond and femtosecond pulsed lasers in particular. Table 9.1 shows a comparison for the minimum incident radiant exposures generating SC at the retina to the MPEs allowed using the ANSI standard.

λ (nm)	β_α (cm^{-1})	Minimum Incident Radiant Exposure H_0 for SC Generation (μJ cm^{-2})	Calculated Maximum Permissible Exposure (MPE) using ANSI Standard	Maximum Permissible Exposure (MPE) values from LHAZ (μJ cm^{-2})	Ratio of calculated ANSI MPE to Minimum Incident Radiant Exposure required for SC Generation
1200	1.27	0.411	0.794 μJ cm^{-2}	0.801	1.932
1250	1.08	0.795	0.9 μJ cm^{-2}	0.9	1.132
1300	1.38	1.502	10.8 μJ cm^{-2}	10.8	7.190
1350	3.48	1.050	1.0 mJ cm^{-2}	164.9	952.381
1400	19.1	5.083	100.0 μJ cm^{-2}	0.01	19.673

TABLE 9.1 Minimum incident radiant exposures for SC generation at the retina.

All exposure values indicate radiant exposure incident to the cornea. The ratios show the factor by which the calculated ANSI MPEs are larger than the minimum

radiant exposures for SC generation at each wavelength. Any ratio greater than one

indicates a potential hazard. At 1350 nm, for example, the ANSI standard allows

approximately 950 times more incident radiant exposure at the cornea than the minimum

incident radiant exposure required for SC generation at the retina as "eye safe". As we

will see in the coming sections, SC was generated in the water cuvette at much smaller

incident radiant exposures, which translated to even lower incident radiant exposures for

SC generation at the retina. This means that some percentage of the NIR incident

radiant energy, deemed "eye safe" by the ANSI standard calculations, will be converted

to higher photon energy white light, shorter wavelength, on or near the retina (see

Rayleigh range in section 8.2). It is this percentage of higher photon energy white light,

which is more transmissive in all optical components of the eye (see Figure 4.4) than

NIR light, that poses a significant eye safety hazard as will be shown in the following

sections.

9.2   EMISSION SPECTRUMS

Figures 9.1-9 are the emission spectrums for every wavelength involved in this

experiment. The first spectrum was measured in air (no water cuvette in place) and the

second "superbroadened" spectrum is of the incident NIR beam exiting the glass cuvette

after interacting with the water inside and generating SC. Note that after the incident

femtosecond pulsed NIR beam interacts with the water in the cuvette, SC is generated at

and near the focus within the water by nonlinear processes such as SPM. It is important

to note that the energy per pulse entering the cuvette at the specific NIR wavelength in

air, designated by the area under the curve in the "NIR through air" spectrums below, does not increase by broadening to higher photon energies (i.e. shorter wavelengths). In fact, the energy of the pulse is lower upon exiting the back glass wall of the cuvette due to the water absorption within the water filled cuvette. The radiant energy exiting the glass cuvette, which was measured, is distributed over the superbroadened emission spectrum. The area under the curve of the "NIR through water" spectrums represents the radiant energy.

FIGURE 9.1 Emission spectrum in air and through water filled glass cuvette for wavelength 1200 nm.

FIGURE 9.2 Emission spectrum in air and through water filled glass cuvette for wavelength 1250 nm.

FIGURE 9.3 Emission spectrum in air and through water filled glass cuvette for wavelength 1300 nm.

FIGURE 9.4 Emission spectrum in air and through water filled glass cuvette for wavelength 1350 nm.

FIGURE 9.5 Emission spectrum in air and through water filled glass cuvette for wavelength 1400 nm.

FIGURE 9.6 Emission spectrum in air and through water filled glass cuvette for wavelength 1450 nm.
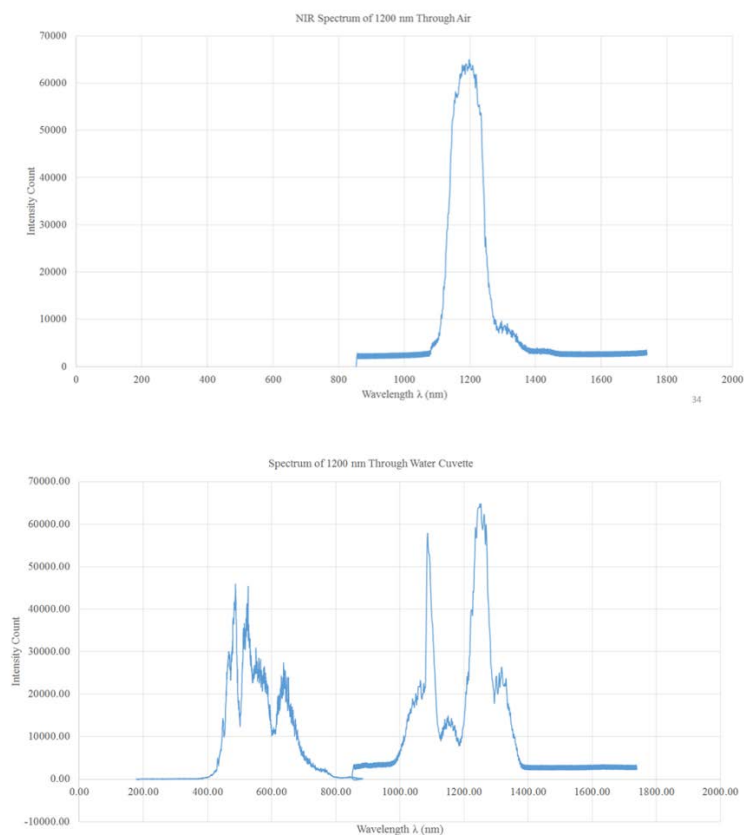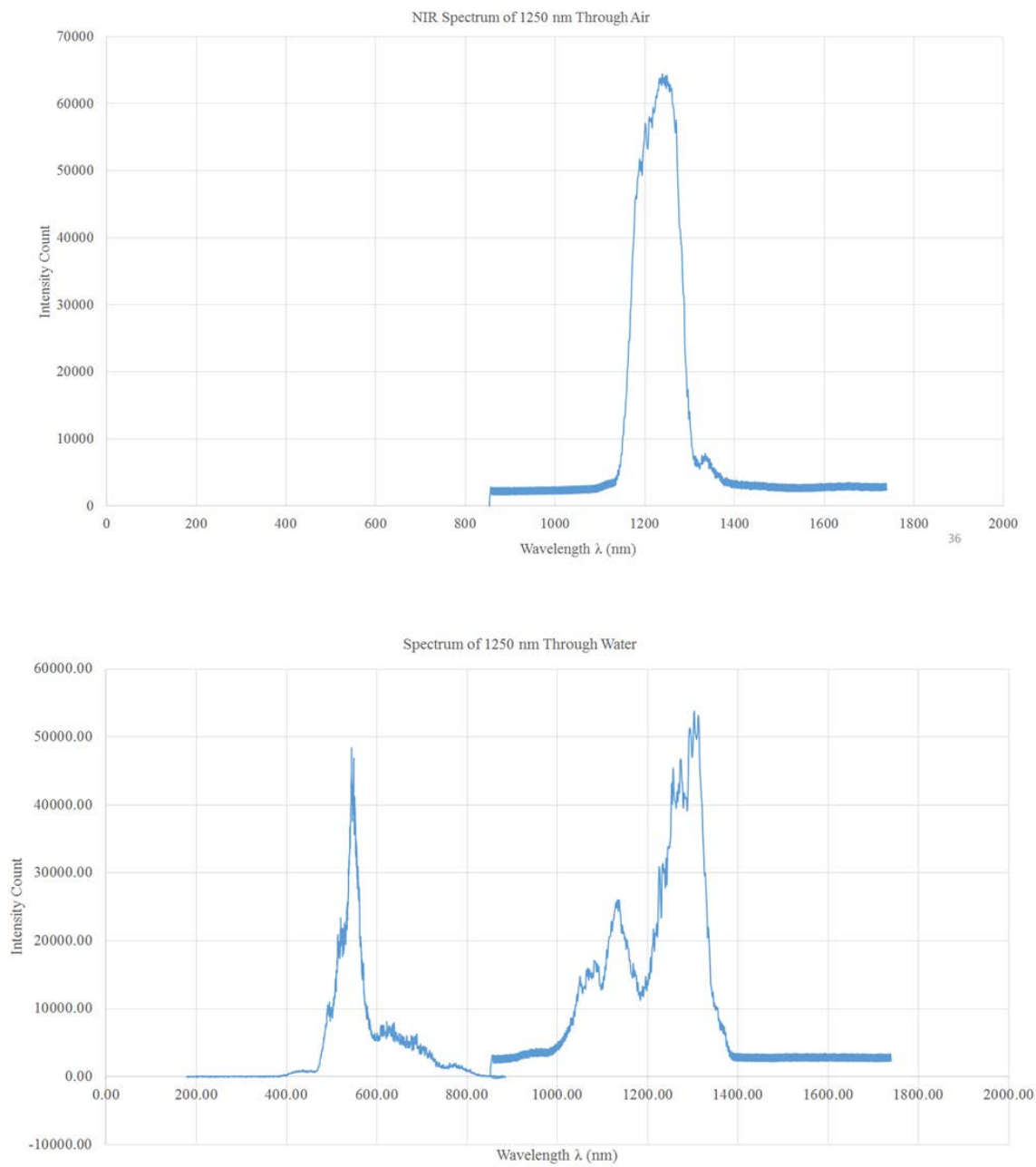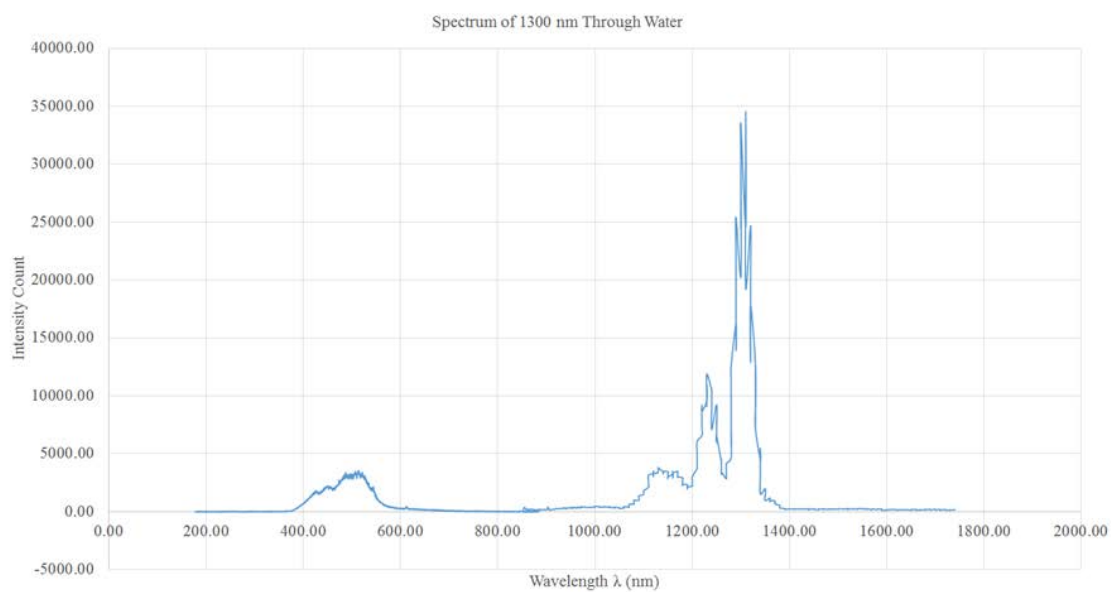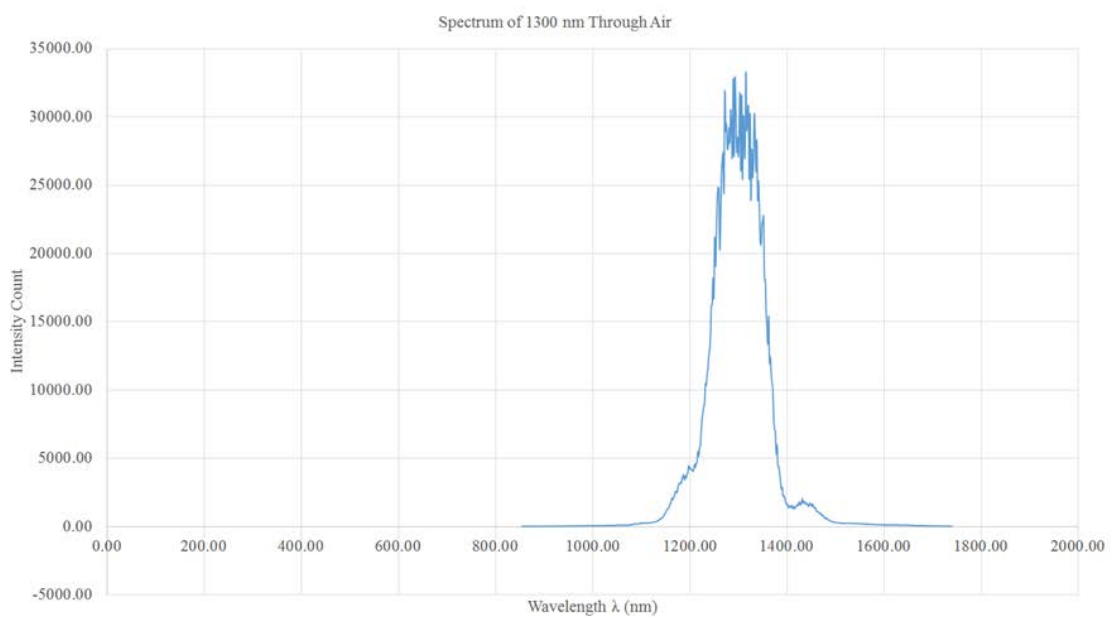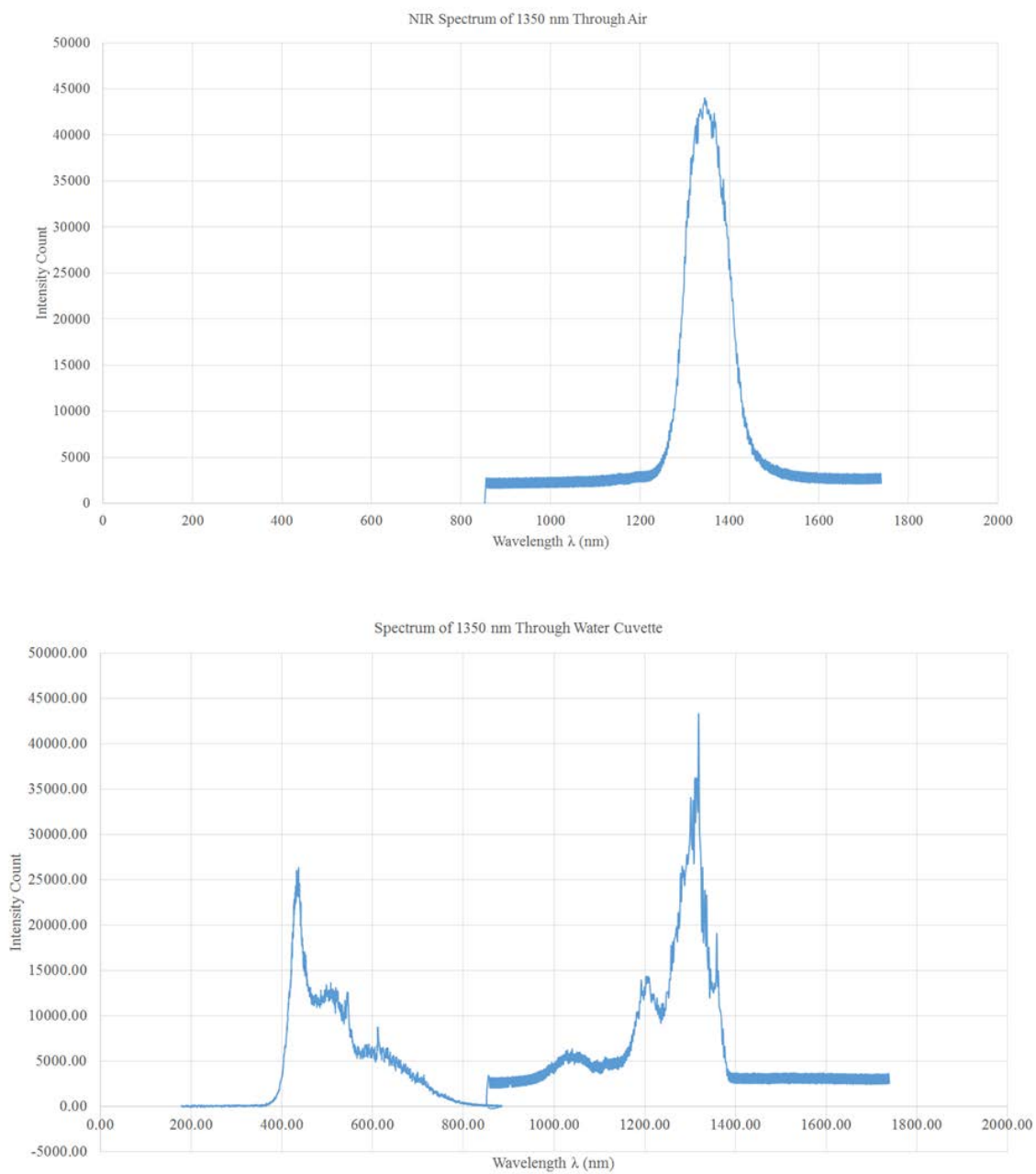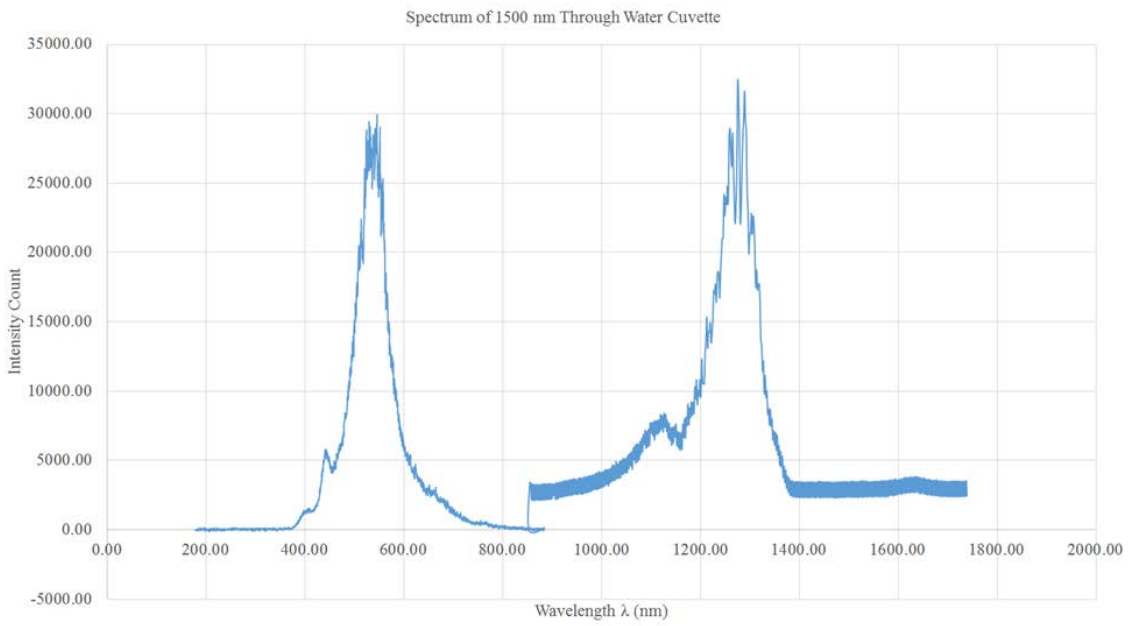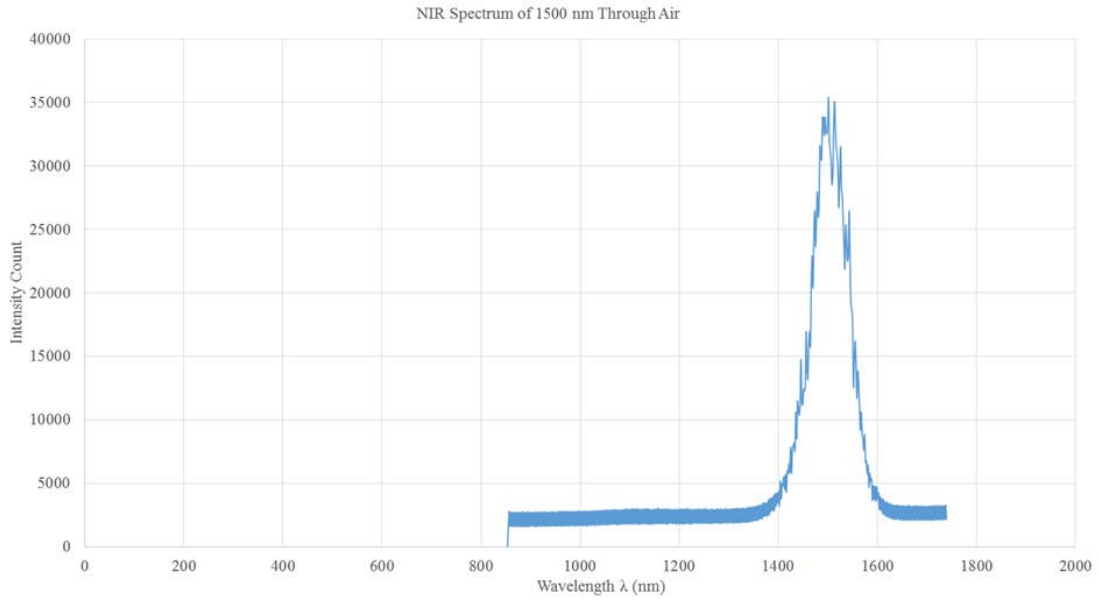
FIGURE 9.7 Emission spectrum in air and through water filled glass cuvette for wavelength 1500 nm.
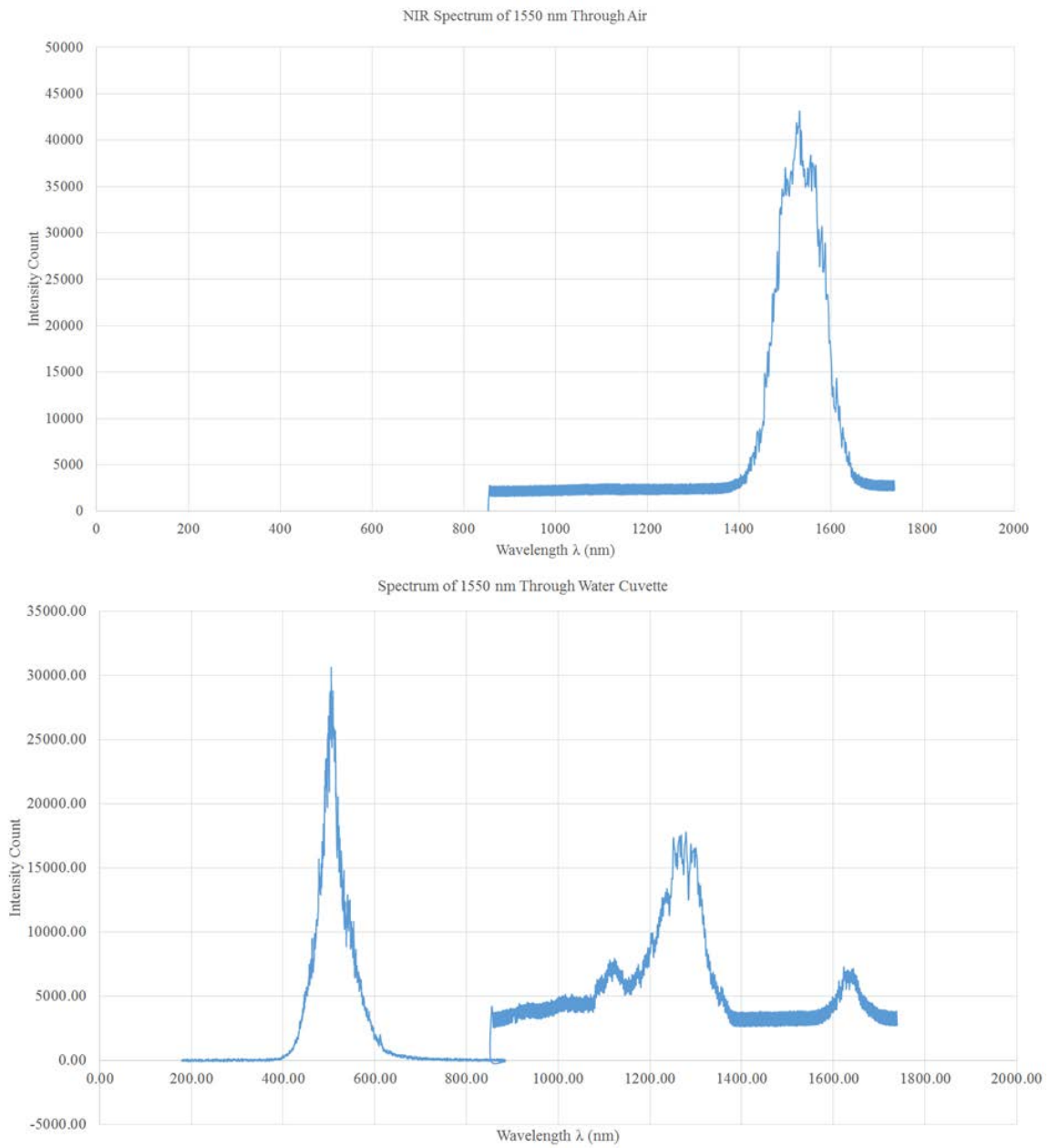
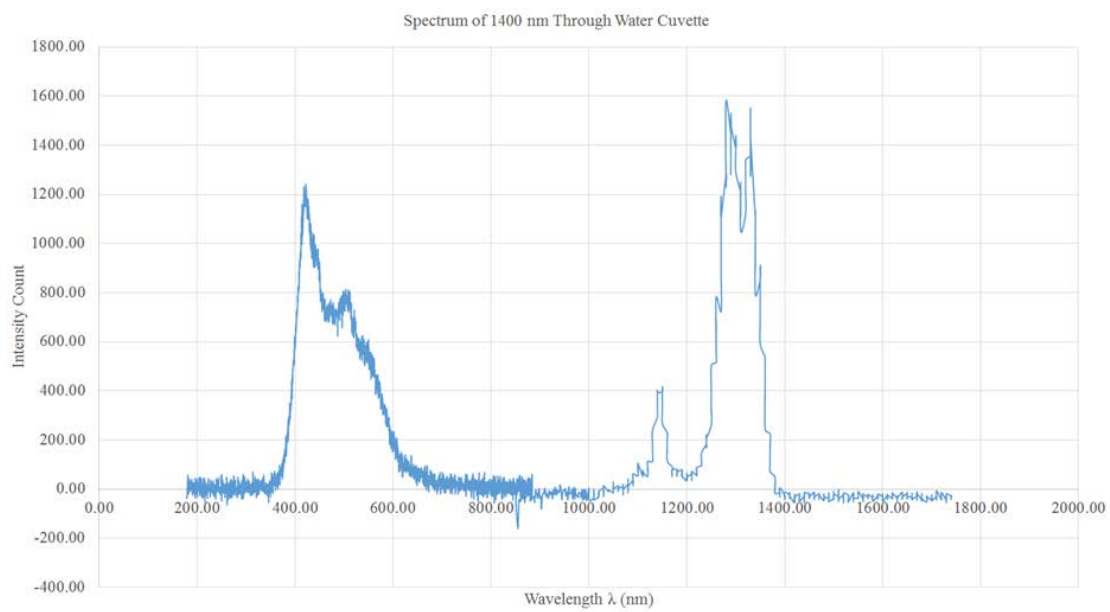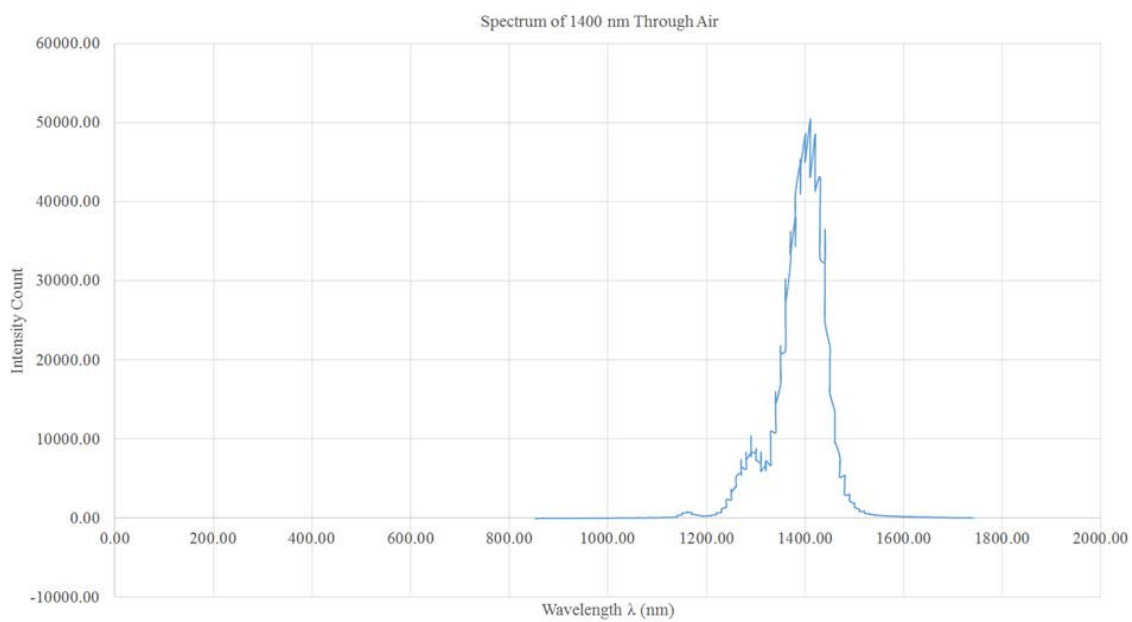FIGURE 9.8 Emission spectrum in air and through water filled glass cuvette for wavelength 1550 nm.
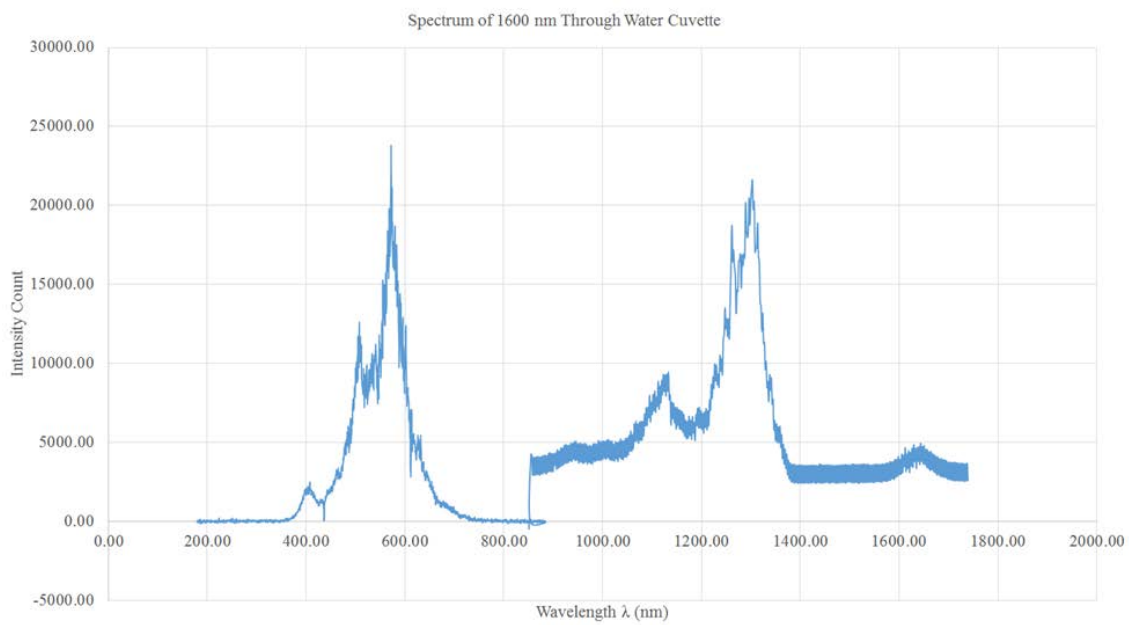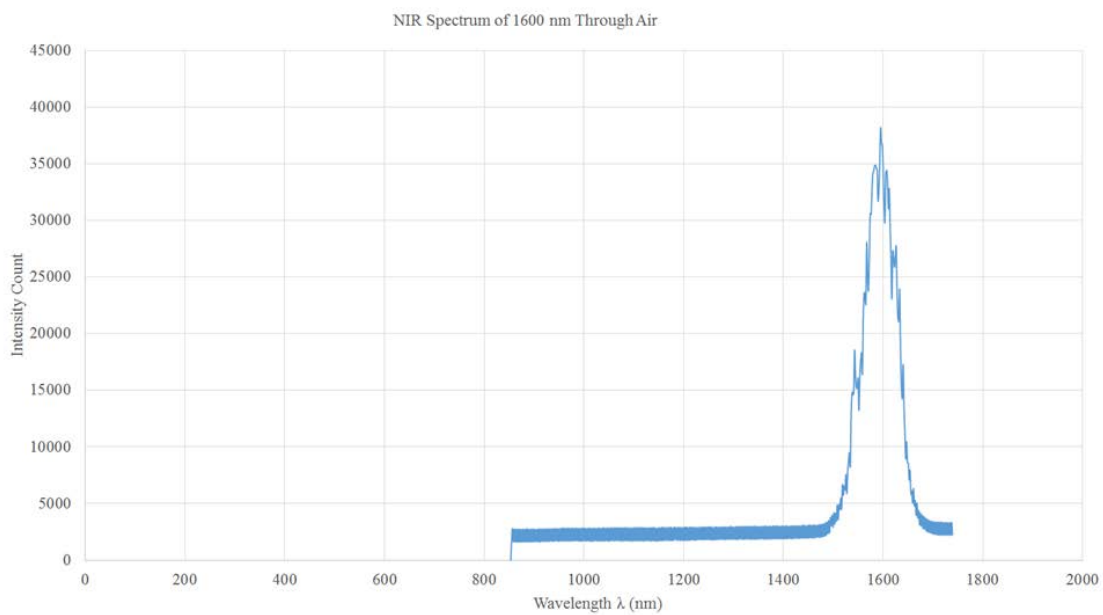
FIGURE 9.9 Emission spectrum in air and through water filled glass cuvette for wavelength 1600 nm.
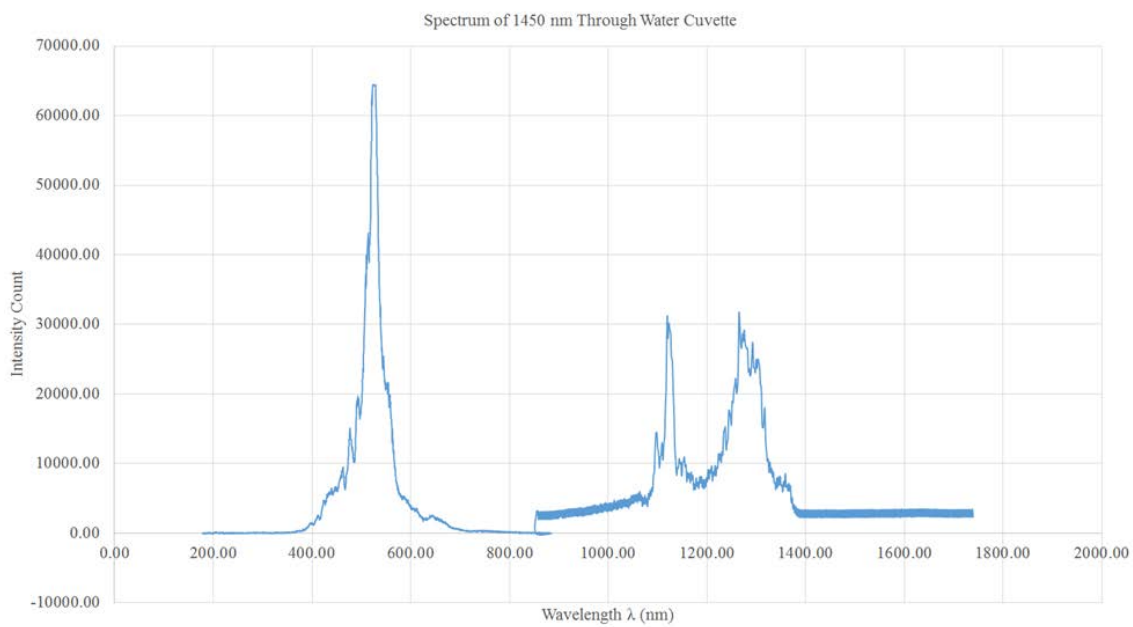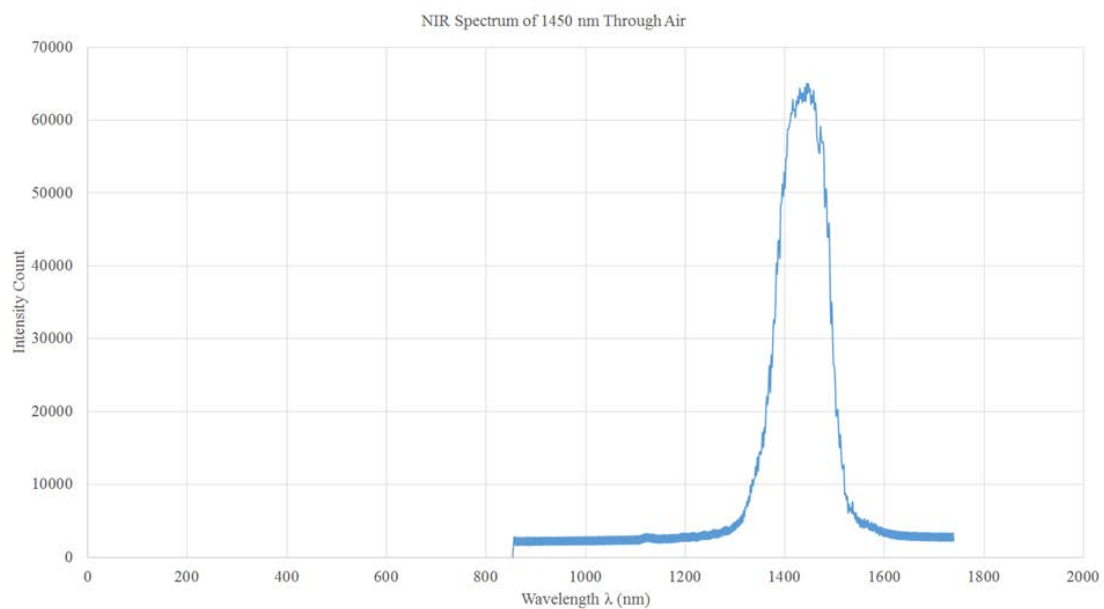
9.3   ESTIMATING WHITE LIGHT RADIANT EXPOSURES

By estimating the percentage of the total area under the curve in the "NIR through water" spectrums above, we can approximate the amount of measured radiant energy exiting the cuvette that has converted to visible white light (400 – 700 nm). We must understand, however, that the measured radiant energy exiting the cuvette is actually less than the radiant energy at the focus, due to the absorption as the beam continues propagating beyond the focus within the water and through the back glass wall of the cuvette. Figure 9.10 estimates the visible white light radiant exposure converted via SC generation for 1200 nm wavelength. Total area under the curve represents approximately 0.469 µJ of energy, approximately 0.188 µJ of which is in the visible spectrum. For the incident 1200 nm NIR laser beam, for example, assuming approximately 40 percent of the measured energy per pulse, E, exiting the water cuvette has converted to the visible spectrum (i.e. 400 to 700 nm), then an approximate 0.188 µJ of energy (likely more at the focus) will be in the visible spectrum. Therefore, at the actual focus located approximately 7.781 mm into the water filled cuvette, the achieved radiant exposure in the 400 nm to 700 nm range will be equal to 5.135 mJ cm^{-2}. Figures 9.11-14 illustrate the SC generated by the 30 to 40 fs NIR pulses for 1250 nm, 1300 nm, 1350 nm, and 1400 nm, respectively. The estimated percentages of exiting energy in the 400 nm to 700 nm range is also listed in each figure. These estimated percentages of white light converted energy in the water cuvette configuration allow for the approximation of white light converted energy in the analysis for the eye configuration.

Spectrum of 1200 nm Through Water Cuvette

λ (nm)	Energy Per Pulse E_0 Entering the Water Cuvette (μJ)	Energy Per Pulse E Exiting the Water Cuvette (μJ)	Approximate Percentage of Exiting Energy in the 400-700 nm Range	Approximate Energy Exiting the Water Cuvette in the 400-700 nm Range (μJ)	γ path length in water cuvette (mm)	Radiant Exposure Achieved in the 400-700 nm Range at the Focus in the Water Cuvette
1200	1.928	0.469	40	0.188	7.781	$5.135 \, \text{mJ cm}^{-2}$

FIGURE 9.10 Estimating the visible white light radiant exposure converted via SC generation for 1200 nm wavelength. Total area under the curve represents approximately 0.469 µJ of energy, approximately 0.188 µJ of which is in the visible spectrum.

Spectrum of 1250 nm Through Water

λ (nm)	Energy Per Pulse E_0 Entering the Water Cuvette (μJ)	Energy Per Pulse E Exiting the Water Cuvette (μJ)	Approximate Percentage of Exiting Energy in the 400-700 nm Range	Approximate Energy Exiting the Water Cuvette in the 400-700 nm Range (μJ)	γ path length in water cuvette (mm)	Radiant Exposure Achieved in the 400-700 nm Range at the Focus in the Water Cuvette
1250	1.653	0.310	30	0.093	7.103	$2.546\,\mathrm{mJ\,cm^{-2}}$

FIGURE 9.11 Estimating the visible white light radiant exposure converted via SC generation for 1250 nm wavelength. Total area under the curve represents approximately 0.310 μJ of energy, approximately 0.093 μJ of which is in the visible spectrum.

Spectrum of 1300 nm Through Water

λ (nm)	Energy Per Pulse E_0 Entering the Water Cuvette (µJ)	Energy Per Pulse E Exiting the Water Cuvette (µJ)	Approximate Percentage of Exiting Energy in the 400-700 nm Range	Approximate Energy Exiting the Water Cuvette in the 400-700 nm Range (µJ)	γ path length in water cuvette (mm)	Radiant Exposure Achieved in the 400-700 nm Range at the Focus in the Water Cuvette
1300	1.616	0.148	20	0.030	7.273	821.226 µJ cm^{-2}

FIGURE 9.12 Estimating the visible white light radiant exposure converted via SC generation for 1300 nm wavelength. Total area under the curve represents approximately 0.148 µJ of energy, approximately 0.030 µJ of which is in the visible spectrum.

76

Spectrum of 1350 nm Through Water Cuvette

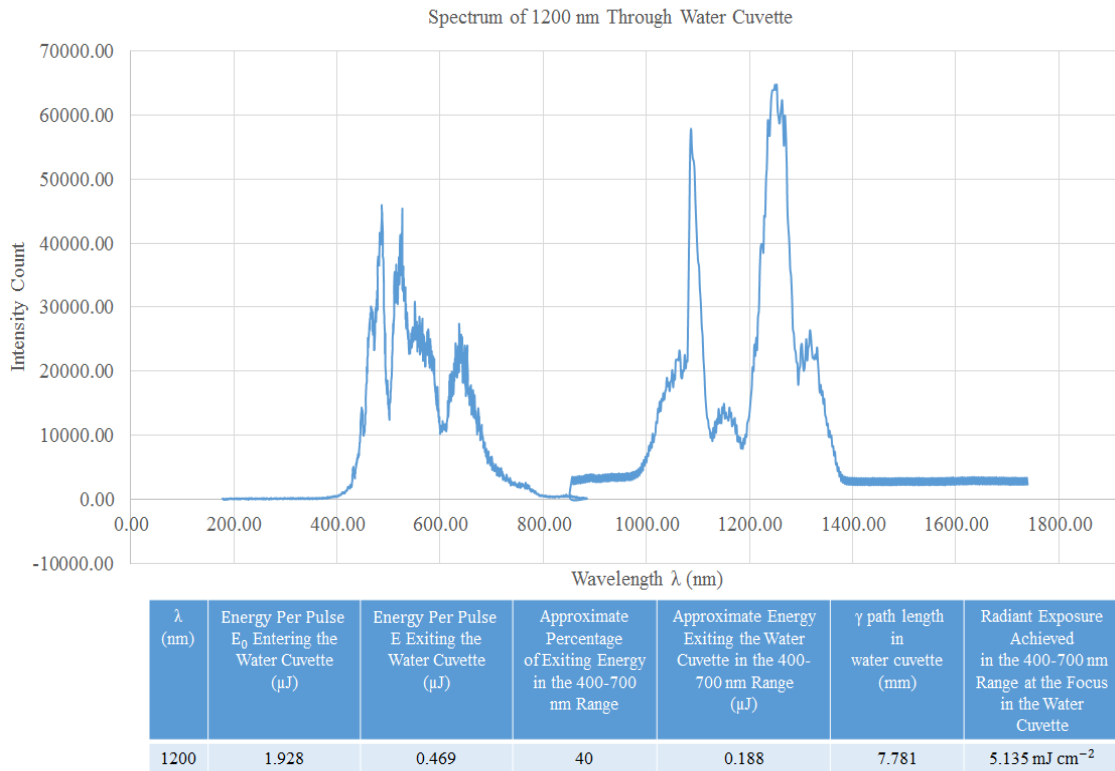| λ (nm)	Energy Per Pulse E_0 Entering the Water Cuvette (µJ)	Energy Per Pulse E Exiting the Water Cuvette (µJ)	Approximate Percentage of Exiting Energy in the 400-700 nm Range	Approximate Energy Exiting the Water Cuvette in the 400-700 nm Range (µJ)	γ path length in water cuvette (mm)	Radiant Exposure Achieved in the 400-700 nm Range at the Focus in the Water Cuvette
1350	1.994	0.109	40	0.044	5.918	$1.190\,\text{mJ cm}^{-2}$

FIGURE 9.13 Estimating the visible white light radiant exposure converted via SC generation for 1350 nm wavelength. Total area under the curve represents approximately 0.109 µJ of energy, approximately 0.044 µJ of which is in the visible spectrum.

Spectrum of 1400 nm Through Water Cuvette

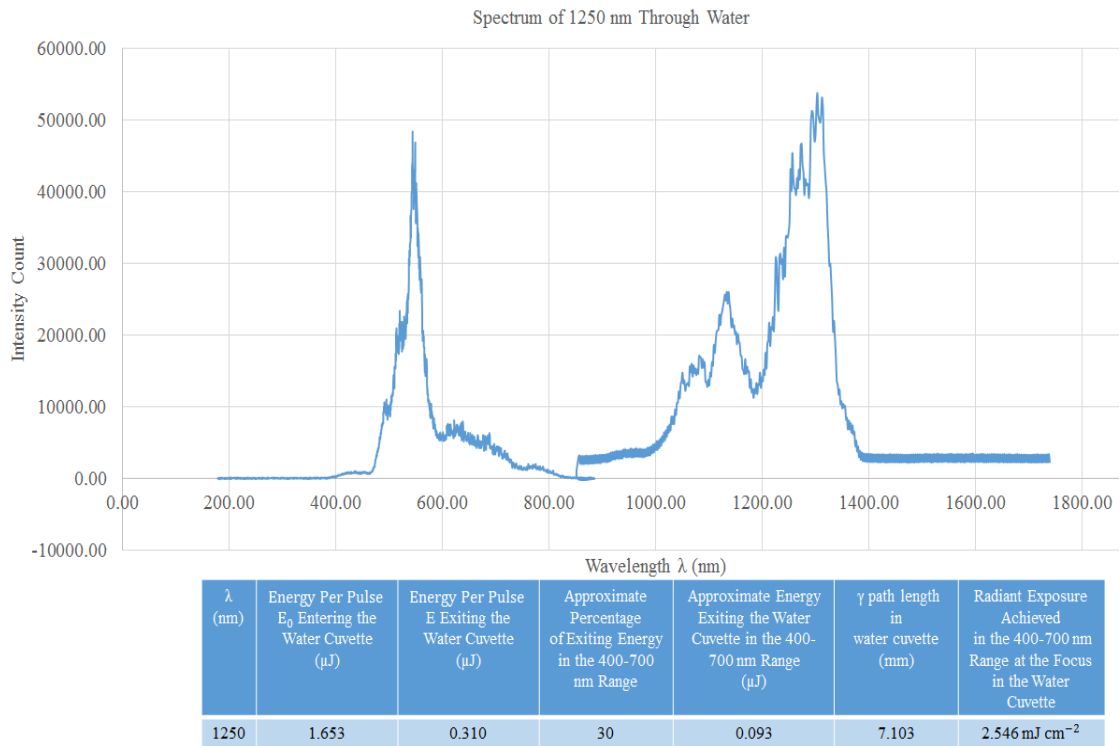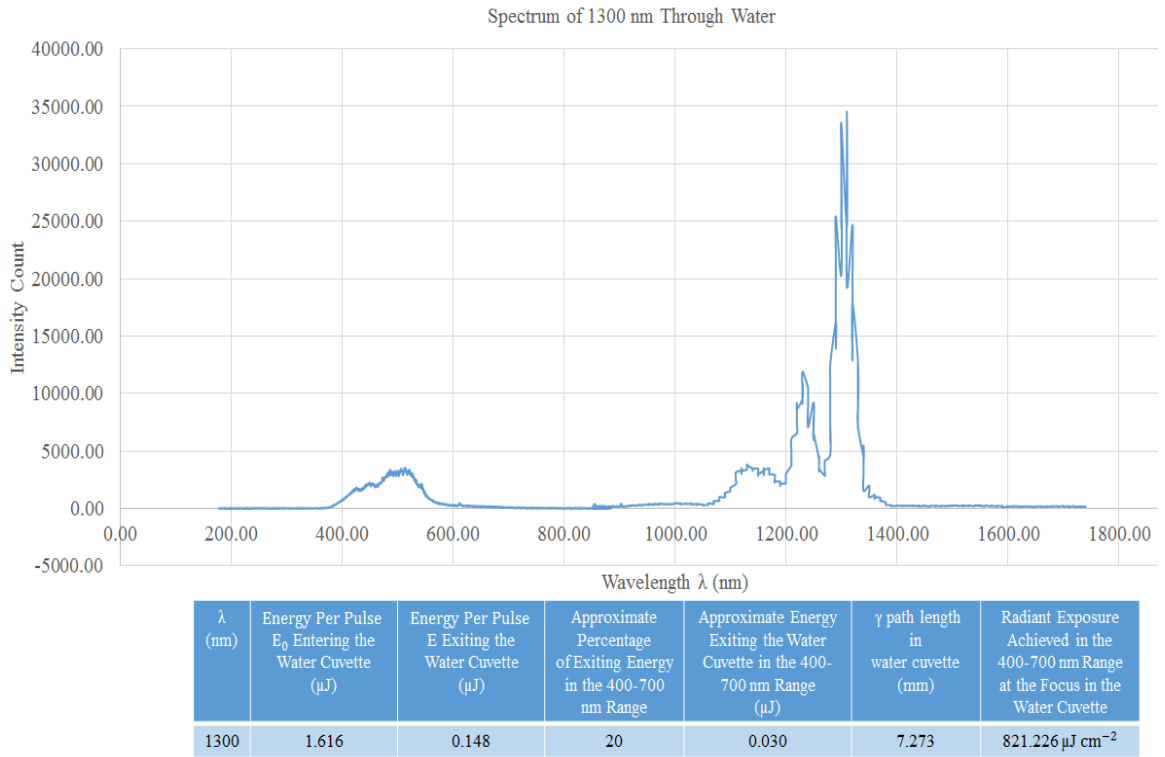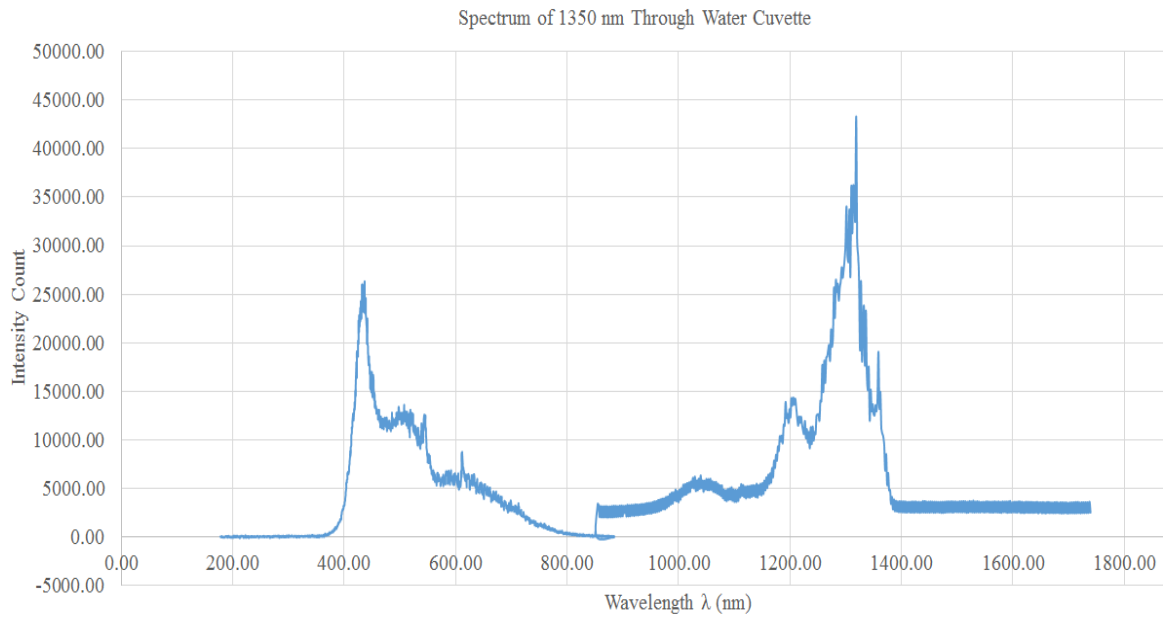| λ (nm)	Energy Per Pulse E_0 Entering the Water Cuvette (µJ)	Energy Per Pulse E Exiting the Water Cuvette (µJ)	Approximate Percentage of Exiting Energy in the 400-700 nm Range	Approximate Energy Exiting the Water Cuvette in the 400-700 nm Range (µJ)	γ path length in water cuvette (mm)	Radiant Exposure Achieved in the 400-700 nm Range at the Focus in the Water Cuvette
1400	3.661	0.107	50	0.054	7.442	$1.461\ \text{mJ cm}^{-2}$

FIGURE 9.14 Estimating the visible white light radiant exposure converted via SC generation for 1400 nm wavelength. Total area under the curve represents approximately 0.107 µJ of energy, approximately 0.054 µJ of which is in the visible spectrum.

Table 9.2 lists the approximate percentages of the areas under the curves for the "NIR through water" spectrums (Figures 9.10-14) that are in the visible wavelength range. Assuming the percentage of converted radiant energy to white light will be similar for the eye configuration as for the water cuvette configuration, we can use the maximum radiant exposures achieved at the retina listed in Table 8.5 to approximate the amount of radiant exposure converted to white light at or near the retina. Using the appropriate percentage of maximum radiant exposure achieved at the retina that has been converted to white light, we get the approximate radiant exposure at the retina in the 400

λ (nm)	Minimum Incident Energy E_0 for SC Generation (μJ)	Minimum Incident Radiant Exposure H_0 for SC Generation (μJ cm^{-2})	Maximum Radiant Exposure H achieved at the retina (i.e. at the focus spot on the retina)	Approximate Percentage of Radiance in the 400-700 nm Range	Approximate Radiant Exposure at the retina in the 400-700 nm Range	Maximum Permissible Exposure (MPE) using ANSI Standard for 400-700 nm (μJ cm^{-2})
1200	0.158	0.411	9.546 mJ cm^{-2}	40	3.818 mJ cm^{-2}	0.1
1250	0.306	0.795	29.170 mJ cm^{-2}	30	8.751 mJ cm^{-2}	0.1
1300	0.578	1.502	26.820 mJ cm^{-2}	20	5.364 mJ cm^{-2}	0.1
1350	0.404	1.050	121.357 μJ cm^{-2}	40	48.543 μJ cm^{-2}	0.1
1400	1.956	5.083	3.078x10^{-14} μJ cm^{-2}	50	1.539x10^{-14} μJ cm^{-2}	0.1

TABLE 9.2 List of approximate radiant exposures at the retina in the 400 to 700 nm range converted from incident NIR wavelengths of 1200 nm, 1250 nm, 1300 nm, 1350 nm, and 1400 nm. Also shown for comparison are the MPEs using the ANSI standard for 400 to 700 nm.

to 700 nm wavelength range for each wavelength listed in Table 9.2. Comparing these

values to the ANSI standard MPEs for the 400 to 700 nm wavelength range, we can

easily observe that the approximate radiant exposure that has been converted to white

light (i.e. 400 to 700 nm) in the vitreous humor (at or near the retina) greatly exceeds the

ANSI standard MPEs, especially for incident wavelengths of 1200 nm, 1250 nm, and

1300 nm. This strongly implies the possibility of retinal damage! The exception is the

incident NIR wavelength of 1400 nm, where the approximate radiant exposure at the

retina that has been converted to white light is approximately 10^{-13} times smaller than the

ANSI standard listed in Table 9.2.
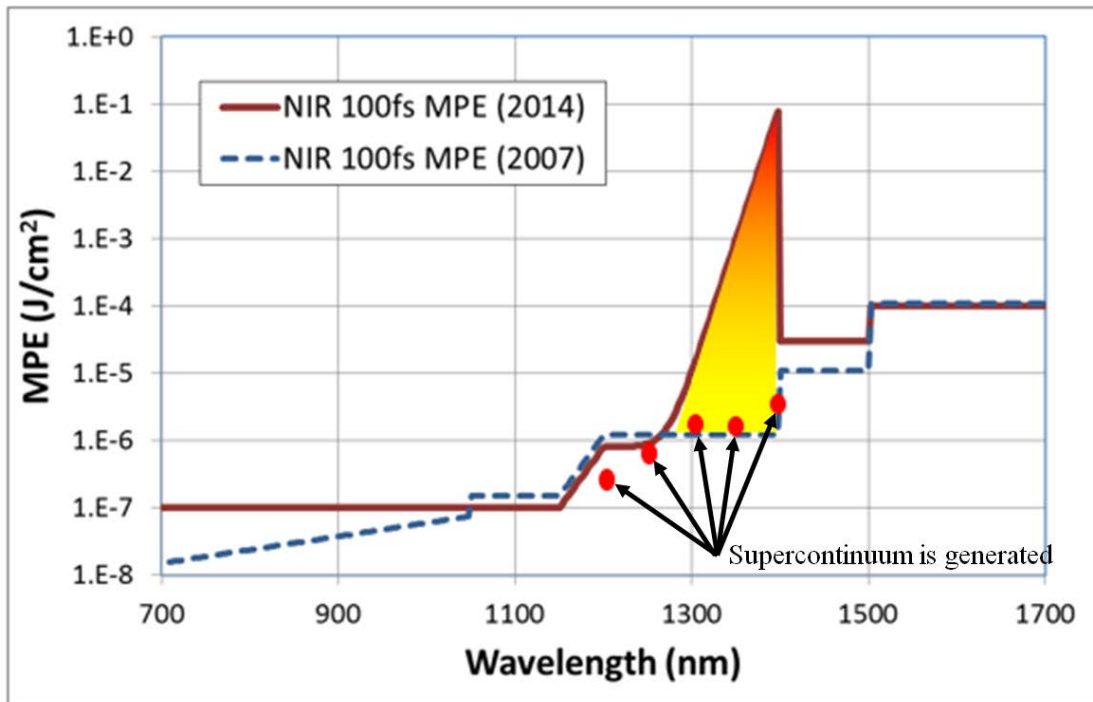
FIGURE 9.15 Minimum radiant exposure values for SC generation compared to the
ANSI 2007 and 2014 MPEs for 100 fs pulsed lasers in the NIR wavelength range.
Percent error is approximately 15 percent or the approximate width of each point.

Figure 9.15 illustrates the minimum incident radiant exposure values that generate SC for NIR wavelengths of 1200 nm, 1250 nm, 1300 nm, 1350 nm, and 1400 nm in the vitreous humor at or near the retina. The percent error of the radiant exposure thresholds generating SC shown in Figure 9.15 is approximately 15 percent for each wavelength, which results in the approximate width of the points shown due to the logarithmic scaling of Figure 9.15. Comparing these minimum incident radiant exposure values to the ANSI 2014 MPE thresholds at these wavelengths clearly illustrates that SC is in fact generated at radiant exposures well below the MPEs for 100 fs pulsed NIR wavelengths.

CHAPTER X

CONCLUSIONS

The primary conclusion of this dissertation is that nonlinear phenomena, specifically SC generation, should be considered for picosecond and femtosecond pulsed lasers when establishing MPEs for eye safety. While this study examined 30 – 40 fs pulsed lasers for the NIR wavelengths of 1200 nm to 1600 nm in 50 nm increments, the relevant wavelengths (for MPEs used for eye safety) only included the wavelengths of 1200 nm, 1250 nm, 1300 nm, 1350 nm, and 1400 nm because wavelengths above 1400 nm are strongly attenuated in the cornea-lens system of the eye. The water cuvette spectral data illustrates the generation of SC for 30 – 40 fs NIR pulsed lasers for the wavelengths and radiant exposures examined in this study. Applying this data to the eye configuration, we were able to calculate estimations that indicate potential retinal hazards that have not been considered in previous studies. While this study does not prove that MVLs will occur at the specific minimum radiant exposures for SC generation shown in Figure 9.15, there is a strong possibility that MVLs may occur below the MPEs listed in the 2014 ANSI standard for 100 fs pulsed NIR lasers at the wavelengths in this research. This study warrants further studies in examining what the effects caused by nonlinear optical phenomena due to ultrashort pulsed lasers (e.g. picosecond and femtosecond) have on MPE thresholds established for eye safety.

REFERENCES

[1]   Rockwell, B.A., Thomas, R.J., Zimmerman, S. "Updates to the ANSI Z136.1 Standard". Proceedings ILSC 2015 (2015).

[2]   Zuclich, J.A., Lund, D.J., Stuck, B.E., Edsall, P.R. "Wavelength dependence of ocular damage thresholds in the near-IR to far-IR transition region (Proposed revisions to MPEs)". Proceedings ILSC 2005 (2005).

[3]   Zuclich, J.A., Lund, D.J., Stuck, B.E. "Wavelength Dependence of Ocular Damage Thresholds in the Near-IR to Far-IR Transition Region: Proposed Revisions to MPEs". Health Physics 92 (1), pp. 15-23 (2006).

[4]   Zuclich, J.A., et al. "Ocular Effects of Penetrating IR Laser Wavelengths". Proceedings SPIE 2391, pp. 112–125 (1995).

[5]   Zuclich, J.A., Schuschereba, S., Zwick, H., Cheney, F.E., Stuck, B.E. "Comparing Laser Induced Retinal Damage from IR Wavelengths to that from Visible Wavelengths". Proceedings SPIE 2674, pp. 66-79 (1996).

[6]   Zuclich, J.A., et al. "A Comparison of Laser-Induced Retinal Damage from Infrared Wavelengths to that from Visible Wavelengths". Lasers Light Ophthalmol 8, pp. 15–29 (1997).

[7]   Zuclich, J.A., Zwick, H., Schuschereba, S.T., Stuck, B.E., Cheney, F.E. "Ophthalmoscopic and Pathologic Description of Ocular Damage Induced by Infrared Laser Radiation". J Laser Applications 10, pp. 114 –120 (1998).

[8]   Zuclich, J.A., Lund, D.J., Edsall, P.R., Stuck, B.E., Hengst, G.T. "High-Power Lasers in the 1.3 to 1.4 µm Wavelength Range: Ocular Effects and Safety Standards Implications". Proceedings SPIE 4246, pp. 78–88 (2001).

[9]   Zuclich, J.A., Lund, D.J., Stuck, B.E., Edsall, P.R. "Ocular Effects and Safety Standards Implications for High-Power Lasers in the 1.3–1.4 µm Wavelength Range". Brooks City-Base, TX: Air Force Research Laboratory, Optical Radiation Branch; AFRL-HE-BR-TR-2004-0187 (2004).

[10]   Zuclich, J.A., Lund, D.J., Stuck, B.E. "Wavelength Dependence of Ocular Damage Thresholds in the Near-IR to Far-IR Transition Region (Proposed Revision to MPEs)". Proceedings International Laser Safety Conference, Marina del Rey. Orlando, FL. Laser Institute of America pp. 58–66 (2005).

[11]   Vincelette, R., et al. "Trends in Retinal Damage Thresholds from 100-Millisecond Near-Infrared Laser Radiation Exposures: A Study at 1,110, 1,130, 1,150, and 1,319 nm". Las. Surg. Med. 41, pp. 382–390 (2009).

[12]   Rockwell, B.A., Thomas, R.J., Vogel, A. "Ultrashort Laser Pulse Retinal Damage Mechanisms and Their Impact on Thresholds". Medical Laser Appl. 25 (2), pp. 84-92 (2010).

[13]   Boyd, R.W. "Nonlinear Optics". Academic press, (2003).

[14]   Rockwell, B.A., Kennedy, P. K., Thomas, R.J., Roach, W.P., Rogers, M.E. "The Effect of Nonlinear Optical Phenomena on Retinal Damage". SPIE Laser-Tissue Interaction VI, 2391A-09, pp. 89-95 (1995).

[15]   ANSI Z136.1-2014 Laser Safety Standard for the Safe Use of Lasers, Laser
        Institute of America, Orlando, Florida (2014).

[16]   Maher, E.F. "Transmission and Absorption Coefficients for Ocular Media of the
        Rhesus Monkey". SAM-TR-78-32. School of Aerospace Medicine. Brooks
        AFB, TX (1978).

[17]   Laser Institute of America. American National Standard for Safe Use of Lasers.
        B3 Example of MPE Determination pp. 118 (2014).

[18]   Hecht, E. Optics. 3rd Edition, pp. 85-87 (1998).

[19]   Raman, C.V. "A New Radiation". Indian J. Phys. 2, pp. 387-398 (2015).

[20]   Baum, P., Lochbrunner, S., Krok, P., Breuer, M., Riedle, E. "NOPA-Overview
        and Principles". BioMolecular Optics (2002).

[21]   Hecht, E. Optics. 3rd Edition p. 250 (1998).

[22]   Hecht, E. Optics. 3rd Edition p. 464 (1998).

[23]   Cain, C., et al. "Artificial Eye for In Vitro Experiments of Laser Light
        Interaction with Aqueous Media". Journal of Biomedical Optics 2 (1), pp. 88-94
        (1997).

[24]   Garlington, T., Babbitt, J., Long, G. "Analysis of Free Space Optics as a
        Transmission Technology". WP No. AMSEL-IE-TS-05001. U.S. Army
        Information Systems Engineering Command (2007).

[25]   Hecht, E. Optics. 3rd Edition p. 634 (1998).

[26]   Chiao, R.Y., Townes, C.H., Stoicheff, B. P. "Stimulated Brillouin scattering and coherent generation of intense hypersonic waves". Phys. Rev. Lett., 12, p. 592 (1964).

[27]   Cumberbatch, E. "Self-focusing in Nonlinear Optics". J. Inst. Maths Applics 6, p. 250 (1970).

[28]   Krause, J.L., Schafer, K.J., Kulander, K.C. "High-order harmonic generation from atoms and ions in the high intensity regime". Phys. Rev. Lett., 68, p. 3535 (1992).

[29]   Alfano, R., Shapiro, S. "Observtion of Self-Phase Modulation and Small-Scale Filaments in Crystals and Glasses". Phys. Rev. Lett. 24 (11), p. 592 (1970).

[30]   New, G. Introduction to Nonlinear Optics. Cambridge University Press. ISBN 978-1-139-50076-0 (2011).

[31]   Tomlinson, W. "Curious Features of Nonlinear Pulse Propagation in Single-Mode Optical Fibers". Optics News 15 (1), pp. 7-11 (1989).

[32]   Laser Biological Hazards-Eyes. Laser Safety Training. Oregon State University, Corvallis, OR. (2015).

[33]   Jones, W.J., Stoicheff, B.P. "Inverse Raman Spectra: Induced Absorption and Optical Frequencies". Phys. Rev. Lett. 13, pp. 657-659 (1964).

[34]   Mash, D.I., Morozav, V.V., Starunov, V.S., Fabelinskii, I.L. "Stimulated Scattering and Spectral Broadening of a High-Power Laser Pulse in Gases". Soviet Physics, JETP Vol. 28, p. 1085 (1965).

[35]   Bloembergen, N., Lallemand, P. "Self-Focusing of Laser Beams and Stimulated
         Raman Gain in Liquids". Phys. Rev. Lett. 15, pp. 1010-1012 (1965).

[36]   Lallemand, P. "Temperature Variation of the Width of Stimulated Raman Lines
         in Liquids". Appl. Phys. Lett. 8, p. 276 (1966).

[37]   Smith, W.L., Liu, P., Bloembergen, N. "Superbroadening in H_2O and D_2O by
         Self-Focused Picosecond Pulses from a YAlG:Nd Laser". Physical Review A,
         Vol. 15, Num. 6, pp. 2396-2404 (1977).

[38]   Alfano, R.R., Shaprio, S.L. "Emission in the Region 4000 to 7000 Å Via Four-
         Photon Coupling in Glass". Phys. Rev. Lett. 24, p. 584 (1970).

[39]   Zheltikov, A.M. "Let There Be White Light: Supercontinuum Generation by
         Ultrashort Laser Pulses". Physics-Uspekhi 49 (6), pp. 605-628 (2006).

[40]   Vasa, P., et. al "Supercontinuum Generation in Water by Intense, Femtosecond
         Laser Pulses Under Anomalous Chromatic Dispersion". Physical Review A 89
         (4), p. 3834 (2014).

[41]   Berger, E. "New Technology Could Capture Solar Energy Now Wasted".
         Houston Chronicle (2011).

[42]   Dilworth, D. "Atmospheric Opacity (Microwaves are around 1 millimeter)".
         Cosmology Science (2012).

[43]   Laser Biological Hazards-Eyes. Laser Safety Training. Oregon State University,
         Corvallis, OR. (2015).

[44]   Miroslaw, J. "Absorption Coefficient of Water: Data Sources." Topics in
         Particle and Dispersion Science (2006).

[45]   Deposit Photos. Vector ID 32339283 (2013).

[46]   Safety of Laser Products-Part 1: Equipment Classification and Requirements, 2nd Edition. International Electrotechnical Commission (2007).

[47]   National Keratoconus Foundation. "How Does The Human Eye Work?" (1998-2014).